

The Impact of Assimilating Satellite-Derived Layered Precipitable Water, Cloud Water Path, and Radar Data on Short-Range Thunderstorm Forecasts

SIJIE PAN,^{a,b,c} JIDONG GAO,^d THOMAS A. JONES,^{a,d} YUNHENG WANG,^{a,d} XUGUANG WANG,^b AND JUN LI^e

^a *Cooperate Institute for Mesoscale Meteorological Studies, University of Oklahoma, Norman, Oklahoma*

^b *School of Meteorology, University of Oklahoma, Norman, Oklahoma*

^c *NOAA/OAR/National Severe Storms Laboratory, Norman, Oklahoma*

^d *NOAA/National Severe Storms Laboratory, Norman, Oklahoma*

^e *Cooperative Institute for Meteorological Satellite Studies, University of Wisconsin–Madison, Madison, Wisconsin*

(Manuscript received 13 February 2020, in final form 19 January 2021)

ABSTRACT: With the launch of *GOES-16* in November 2016, effective utilization of its data in convective-scale numerical weather prediction (NWP) has the potential to improve high-impact weather (HIWeather) forecasts. In this study, the impact of satellite-derived layered precipitable water (LPW) and cloud water path (CWP) in addition to NEXRAD observations on short-term convective-scale NWP forecasts are examined using three severe weather cases that occurred in May 2017. In each case, satellite-derived CWP and LPW products and radar observations are assimilated into the Advanced Research Weather Research and Forecasting (WRF-ARW) Model using the NSSL hybrid Warn-on-Forecast (WoF) analysis and forecast system. The system includes two components: the GSI-EnKF system and a deterministic 3DEnVAR system. This study examines deterministic 0–6-h forecasts launched from the hybrid 3DEnVAR analyses for the three severe weather events. Three types of experiments are conducted and compared: (i) the control experiment (CTRL) without assimilating any data, (ii) the radar experiment (RAD) with the assimilation of radar and surface observations, and (iii) the satellite experiment (RADSAT) with the assimilation of all observations including surface-, radar-, and satellite-derived CWP and LPW. The results show that assimilating additional GOES products improves short-range forecasts by providing more accurate initial conditions, especially for moisture and temperature variables.

KEYWORDS: Radars/Radar observations; Satellite observations; Sensitivity studies; Numerical weather prediction/forecasting; Data assimilation

1. Introduction

Many studies have demonstrated that high-resolution radar data from the WSR-88D network (Crum et al. 1993), play a pivotal role in convective-scale data assimilation and numerical weather prediction (NWP) since these data provide three-dimensional internal structures of storms (Dowell et al. 2004; Gao et al. 2004; Sun 2005; Aksoy et al. 2009; Stensrud and Gao 2010; Yussouf and Stensrud 2010; Dowell et al. 2011; Gao and Stensrud 2012; Yussouf et al. 2013; Johnson et al. 2015; Wheatley et al. 2015; Gao et al. 2016; Wang and Wang 2017). However, challenges of assimilating high-density radar observations have also been exposed. Only information about wind and some hydrometeor variables within storms can be directly detected by radars, while information about these variables outside storms, and other model variables (e.g., temperature and specific humidity) are not generally detected. As a result, large errors and biases in the initial conditions, especially for moisture and related thermodynamic variables, remain one of the major hurdles in properly predicting the location, timing, and intensity of potentially dangerous severe weather events (Stensrud and Gao 2010; Parker 2014).

With the launch of *GOES-16* of the new generation of Geostationary Operational Environmental Satellite (GOES-R series), assimilating satellite observations, or derived products into convective-scale NWP has become more attractive. Some

studies suggested that additional satellite observations can partially compensate the limitation of assimilating only radar observations (Jones et al. 2013; Fierro et al. 2016; Jones et al. 2016, 2018, 2020; Fierro et al. 2019; Zhang et al. 2019; Hu et al. 2020). One of the applications of assimilating satellite-derived products in convective-scale NWP has been studied by Jones et al. (2013). In their experiments, both radar observations and satellite product cloud water path (CWP) were assimilated into the three-dimensional compressible nonhydrostatic WRF model with the Advanced Research WRF (ARW) dynamic solver (WRF-ARW; Skamarock et al. 2008) for predicting a severe weather event that occurred on 10 May 2010. Their experiments showed that the assimilation of CWP resulted in improvements in cloud properties and more accurate short-wave radiation flux at the surface by comparing to the experiments without CWP assimilation. Although this positive impact decreases with increasing lead time, the benefits were still maintained 90 min into the model simulation.

Pan et al. (2018) explored the benefit of assimilating another satellite product, total precipitable water (TPW), in addition to CWP and radar data, in an idealized case study using a three-dimensional ensemble-variational (3DEnVar) system (Gao et al. 2016). In this idealized case study, the forecasts that assimilated TPW in addition to radar data were more accurate than those that assimilated only radar observations. Wang et al. (2018) also found that the assimilation of the three-layer precipitable water product derived from the Advanced Himawari Imager (AHI) in regional NWP improved heavy precipitation

Corresponding author: Sijie Pan, sijie.pan@noaa.gov

DOI: 10.1175/MWR-D-20-0040.1

© 2021 American Meteorological Society. For information regarding reuse of this content and general copyright information, consult the [AMS Copyright Policy](#) (www.ametsoc.org/PUBSReuseLicenses).

forecasts, especially when the assimilation was combined with appropriate cumulus and microphysical schemes (Lu et al. 2019). Based on these findings, we believe that the assimilation of satellite derived water related products has the potential to improve convective-scale NWP by providing more accurate model initial conditions especially for moisture and thermodynamic variables.

The layered precipitable water (LPW) is one of the products of the newly launched *GOES-16* and *GOES-17*, and its usefulness to convective-scale NWP has not been studied to our knowledge. So in this study, we evaluate the added value of assimilating LPW and CWP products on short-term convective-scale NWP using a hybrid ensemble variational system with several real data cases. Three HIWeather events occurring in May 2017 are assessed (Table 1) by comparing analyses and short-term forecasts from three sensitivity experiments. The first experiment does not assimilate any observations. The second experiment uses only radar and surface observations. The last group of experiments uses satellite-derived CWP and LPW products together with radar observations from WSR-88D network and surface observations. The added value for the assimilation of additional satellite observations can be easily assessed by comparing the above experiments. These three events represent different weather regimes, allowing us to test the applicability and effectiveness of the satellite-derived products in different weather scenarios.

The remainder of this study is organized as follows. Section 2 describes mainly the satellite LPW and CWP products and their associated forward operators and other observations used in the experiments. The hybrid data assimilation method and mode configuration are briefly introduced in section 3. Both analysis and forecast results are detailed in section 4. Section 5 presents a synthesis of the current work followed by concluding remarks and potential future research avenues.

2. Observations used and their associated forward operators

a. Layered precipitable water

The advanced Baseline Imager (ABI) is designed for the GOES-R series that has been launched since 2016. Differing from the GOES Imager carried on GOES-M series, ABI implements more spectral bands as well as higher temporal and spatial sampling capabilities (Schmit et al. 2005, 2017). A new experimental retrieval product, LPW, is available by taking the advantage of extra spectral bands. The retrieval algorithm was developed for deriving legacy atmospheric temperature and moisture profiles from radiance measurements from ABI. It uses the general least squares regression as a first guess followed by a one-dimensional variational approach and retrieves atmospheric temperature and moisture profiles and the derived products, including TPW and LPW from the clear sky infrared radiances (Schmit et al. 2019). The LPW retrieval algorithm mostly depends on the 6.2-, 6.9-, and 7.3- μm infrared bands, which represent the water vapor distribution in upper, mid-, and lower midtroposphere, respectively. It also requires other infrared longwave bands such as 10.3-, 11.2-, 12.3-, and

TABLE 1. List of three high-impact weather events for assessing the impact of assimilating *GOES-13* and *GOES-16* retrieval observations in convective-scale NWP. The 3–6-h forecasts are launched at 1-h intervals from 2000 to 2300 UTC.

Event	Region	Period
10 May 2017	Northern TX/southern OK	2000–0200 UTC
16 May 2017	TX Panhandle/southwestern OK	2000–0100 UTC
26 May 2017	Eastern CO	2000–0100 UTC

13.3- μm bands for cloud-clearing purposes (Schmit et al. 2019). The LPW product is only available over clear-sky areas.

The LPW (in cm) accumulates water vapor contained in a vertical column over a unit cross-sectional area between two specific levels. The forward operator used in our hybrid data assimilation system can be written as follows:

$$\text{LPW} = -\frac{100}{\rho_w g} \int_{\text{low-level}}^{\text{high-level}} q_v(p) dp, \quad (1)$$

where ρ_w is the water density, and q_v is the water vapor mixing ratio. The troposphere is classified into three different PW layers: boundary layer (BL; sigma level: 1.0–0.9), middle layer (ML; sigma level: 0.9–0.7), and high layer (HL; sigma level: 0.7–0.3). Therefore, the atmospheric pressure at a particular sigma level needs to be determined for the LPW calculation based on the following equation:

$$P_{\text{sig}} = P_{\text{top}} + \text{sig_index} \times (P_{\text{sfc}} - P_{\text{top}}), \quad (2)$$

where P_{top} represents the model top pressure, P_{sfc} represents the surface pressure, and sig_index represents the sigma level in model. Once the low-level and high-level pressures for a particular layer have been determined by sigma level, then Eq. (1) is applied to calculate LPW within this layer. In this study, only the BL and ML of the LPW product are utilized since some sensitivity experiments indicate that large forecast biases exist within several 2017 cases when HL precipitable water is involved.

b. Cloud water path from GOES-13 imager measurements

The GOES-M series imager allows sampling of visible and infrared radiation over the continental United States (CONUS) every 5–15 min on an on-demand basis (Menzel and Purdom 1994; Schmit et al. 2001). The CWP is retrieved from GOES-M imager radiances with a 4-km resolution for cloudy pixels using the Visible Infrared Solar-Infrared Split-Window Technique (Minnis et al. 2011). The impact of assimilating these products in an ensemble, convection-allowing NWP system using the ensemble square root filter (EnSRF; Whitaker and Hamill 2002) assimilation method are described in detail by Jones et al. (2013), Jones and Stensrud (2015), and Jones et al. (2016). Parallax correction is performed before the assimilation process so that the locations of clouds are adjusted to their ground-relative coordinates (Jones et al. 2018).

The forward operator for satellite CWP retrievals is defined by Jones and Stensrud (2015). The model equivalent CWP is calculated by integrating total cloud water mixing ratio over the atmospheric column from observed cloud base to cloud top:

$$\text{CWP} = -\frac{1}{g} \int_{\text{CBP}}^{\text{CTP}} \sum_{x=1}^n q_x(p) dp. \quad (3)$$

As shown in Eq. (3), CBP represents the pressure of the cloud base, which is determined by the optical depth and cloud top properties, CTP represents the pressure of the cloud top, p is the atmospheric pressure, q_x is hydrometeor mixing ratio for a specific species (x), and n indicates the number of hydrometeor species based on the microphysics scheme and observed cloud phase. In this study, five resulting hydrometeor variables prognosed by the Thompson 1.5-moment microphysics scheme are adopted. The mass mixing ratios of the five hydrometeor variables (q_c, q_r, q_i, q_s, q_g) are used to create a total cloud water mixing ratio $\sum_{x=1}^n q_x(p)$ at a specific model grid point. As described in Jones and Stensrud (2015), cloud phase at each pixel can be classified as either “liquid” or “ice” based on the cloud temperature and cloud effective particle size information. In the forward operator, CWP represents the column integration of liquid cloud and rain hydrometeors for observed liquid cloud pixel. An “ice” pixel represents the column integration of both liquid and frozen hydrometeors (such as snow, ice, graupel and hail) because the current algorithm for retrieving CWP is unable to separately identify mixed-phase clouds such as deep convective clouds that may contains both liquid and ice phase hydrometeors. The CWP product is generally used to discern cloudy and clear-sky areas in the domain. To partially address the production of spurious clouds and convection in the model domain, our data assimilation procedure also considers the assimilation of zero CWP observations.

c. Radar and surface observation

Radial velocity and reflectivity observations are synthesized by using level II data from the NEXRAD WSR-88Ds within and surrounding the selected domain for each event, and then are interpolated onto the model grids. Radar quality control procedures (such as buddy checking, dealiasing, and anomalous returns removal) are applied before they are assimilated (Gao et al. 2013). The forward operator and its adjoint for reflectivity are the same as those used in Gao and Stensrud (2012), and for radial velocity are same as those used in Gao et al. (2013). Because we omit precipitation terminal velocity from the observed radial velocity prior to the analysis, only the preconditioned control variables (u, v, w) for wind are required to calculate model-derived radial velocity. Surface observations of wind, pressure, temperature and specific humidity extracted from NCEP Meteorological Assimilation Data Ingest System (MADIS) data are assimilated into the data assimilation experiments at 60-min intervals. Although observations from the Oklahoma Mesonet (Mesonet hereafter) are available for some cases, they are not assimilated in this study to aid in the consistency of the results among events.

3. The hybrid system and experimental design

a. The ensemble data assimilation system

The NSSL hybrid system includes two components: the GSI-EnSRF, and a deterministic 3DEnVAR scheme. The GSI-EnSRF is one of the EnSRF systems that has been used for

convective-scale data assimilation in both the operational and research communities (Johnson et al. 2015; Wang and Wang 2017; Jones et al. 2018; Yussouf and Knopfmeier 2019). The ensemble data assimilation system assimilates conventional observations, radar observations and satellite-derived cloud water path, but not LPW because the forward operator for LPW product has not been included in the system yet. Conventional observations have varied localization length from 60 km for the Mesonet to 460 km for the sparser resolution instruments (e.g., the Automated Surface Observing System and the Aircraft Communications Addressing and Reporting System). The radar observations and CWP use 18- and 36-km horizontal radii, respectively. Localization values applied here were derived from those used by Jones et al. (2018). Some very encouraging results have been obtained using this GSI-EnSRF system for convective-scale radar and satellite data assimilation in short-term forecasts in real-time operations (Yussouf and Knopfmeier 2019).

b. The deterministic data assimilation system

The deterministic data assimilation system is the 3DEnVAR system used in Pan et al. (2018) and Wang et al. (2019). The system was based on the ARPS 3DVar (Gao et al. 1999, 2002, 2004; Brewster et al. 2005; Hu et al. 2006; Gao and Stensrud 2012) data assimilation system, which was designed to specifically assimilate radar reflectivity and radial velocity. The static background error covariance matrix is modeled by the product of a diagonal matrix of the standard deviation of the background error and a spatial recursive filter (Gao et al. 2004; Gao et al. 2013). The standard deviations for the model variables are derived from the statistics of the Rapid Update Cycle (RUC, Benjamin et al. 2004) model 3-h forecasts over several years from 2001 to 2004. Multiple passes (or outer loops) can be applied to the recursive filter as proposed by Purser et al. (2003). In this study, two outer loops of the recursive filter are applied. In the first outer loop, surface observations and LPW are assimilated with a 60-km horizontal localization radius. In the second outer loop, radar radial velocity, reflectivity and CWP are assimilated using the 18-km horizontal localization radius. Both inner loops use 40 iterations.

The system has recently been extended to incorporate flow-dependent covariances from the ensemble (Gao and Stensrud 2014; Gao et al. 2016) and to include the required forward operators and their adjoints for assimilating satellite derived products (Fierro et al. 2019; Pan et al. 2018; Hu et al. 2020). Since commonly used background error covariance \mathbf{B} for the traditional 3DVar method is static, it cannot appropriately represent the flow-dependent error growth that relies on the particular atmospheric situation. We implement an alpha control variable method, which was first proposed by Lorenc (2003) to incorporate flow-dependent ensemble covariance into variational methods. As formulated, the 3DVar scheme is renamed as 3DEnVar, in which the background error covariance \mathbf{B} is obtained by combining the static covariance and flow-dependent covariance (Buehner 2005; Wang et al. 2007, 2008; Gao and Stensrud 2014). Based on preliminary sensitivity experiments (not shown), the weight for the flow-dependent

TABLE 2. PBL and radiation scheme combinations for 36 ensemble members of each 2017 event. Deterministic member indicates the extra member used for deterministic analysis and forecast. The PBL schemes include MYJ (Janjić 1994), YSU (Hong et al. 2006), and MYNN2 (Nakanish 2001; Nakanishi and Niino 2004). The radiation schemes include Dudhia (Dudhia 1989), RRTM (Mlawer et al. 1997), RRTMG (Iacono et al. 2008), and Goddard (Chou and Suarez 1999; Chou et al. 2001).

Member	GEFS member	PBL	Shortwave radiation	Longwave radiation
Deterministic	GFS	MYJ	RRTMG	RRTMG
1	1	YSU	Dudhia	RRTM
2	2	YSU	Goddard	Goddard
3	3	MYJ	RRTMG	RRTMG
4	4	MYJ	Dudhia	RRTM
5	5	MYNN2	Goddard	Goddard
6	6	MYNN2	RRTMG	RRTMG
7	7	YSU	Dudhia	RRTM
8	8	YSU	Goddard	Goddard
9	9	MYJ	RRTMG	RRTMG
10	10	MYJ	Dudhia	RRTM
11	11	MYNN2	Goddard	Goddard
12	12	MYNN2	RRTMG	RRTMG
13	13	YSU	Dudhia	RRTM
14	14	YSU	Goddard	Goddard
15	15	MYJ	RRTMG	RRTMG
16	16	MYJ	Dudhia	RRTM
17	17	MYNN2	Goddard	Goddard
18	18	MYNN2	RRTMG	RRTMG
19	1	MYNN2	RRTMG	RRTMG
20	2	MYNN2	Goddard	Goddard
21	3	MYJ	Dudhia	RRTM
22	4	MYJ	RRTMG	RRTMG
23	5	YSU	Goddard	Goddard
24	6	YSU	Dudhia	RRTM
25	7	MYNN2	RRTMG	RRTMG
26	8	MYNN2	Goddard	Goddard
27	9	MYJ	Dudhia	RRTM
28	10	MYJ	RRTMG	RRTMG
29	11	YSU	Goddard	Goddard
30	12	YSU	Dudhia	RRTM
31	13	MYNN2	RRTMG	RRTMG
32	14	MYNN2	Goddard	Goddard
33	15	MYJ	Dudhia	RRTM
34	16	MYJ	RRTMG	RRTMG
35	17	YSU	Goddard	Goddard
36	18	YSU	Dudhia	RRTM

ensemble and static background error covariances in this research is set to 0.6 and 0.4, respectively.

c. Model configurations and experiment design

In each experiment, the ensemble system uses WRF V3.8.1 to generate a 36-member ensemble of storm-scale forecasts for the three events. The initial and boundary conditions are initialized at 1200 UTC using the 1° 6-h global ensemble forecast system (GEFS; Zhou et al. 2017) forecasts, and then 6-h forecasts are launched to spinup finescale structures in the ensemble data assimilation system. The simulations in our data assimilation experiments are performed on a 2-km spaced grid of 480×360 horizontal points resulting in a $960 \text{ km} \times 720 \text{ km}$ domain, and 51 stretched vertical levels reaching up to 50-hPa with a 56–460-m thickness between individual levels. The center of the domain for the relevant event is selected based on

the storm reports provided by the Storm Prediction Center (SPC) so that the principal HIWeather, especially tornadoes, large hail and high winds are located within the domain. Initial and boundary conditions are provided by the first 18 members of the 21-member GEFS. In addition to the initial and boundary conditions, variations in boundary layer physics and radiation schemes are applied to create a different set of model physics for each ensemble member to avoid underdispersion between members (Stensrud et al. 2000; Fujita et al. 2007; Wheatley et al. 2014).

The combinations of PBL and radiation schemes for the ensemble members are shown in Table 2, similar to those described in Wheatley et al. (2015) and Skinner et al. (2018). The same combinations of the parameterization schemes are applied to the reverse order of downscaled GEFS members to create the remaining 18 ensemble members so that member 19

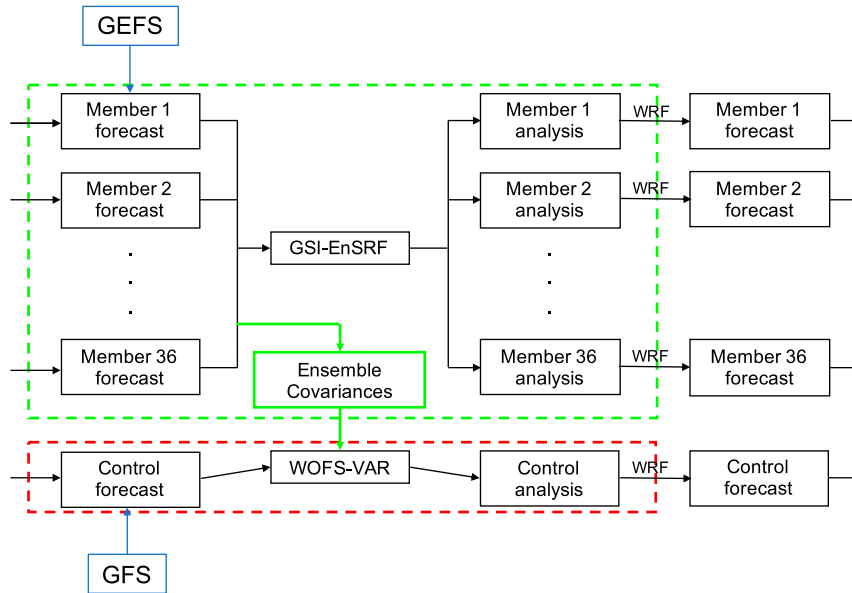


FIG. 1. Schematic diagram of a single hybrid 3D-EnVar data assimilation cycle [modified based on Fig. 1a of Wang et al. (2013)].

is obtained by downscaling GEFS member 18 but using the parameterization combination for member 1. All ensemble members adopt the Thompson cloud microphysics scheme (Thompson et al. 2004, 2008). Because the simulations are performed on a 2-km convection-allowing grid, no cumulus parameterization scheme is used. Although the multiplicative covariance inflation method is not applied to the system (Jones et al. 2018), the additive noise technique described in Dowell and Wicker (2009) is applied to maintain the spread between ensemble members. Local perturbations are added to temperature (0.5 K), dewpoint temperature (0.5 K), and wind (0.5 m s^{-1}) for the grid points where $>25\text{-dBZ}$ reflectivity is observed and the absolute innovation of the posterior ensemble mean reflectivity is less than 10 dBZ. Zero reflectivities are assimilated in the GSI-EnSRF scheme to suppress spurious precipitation.

As described in Fig. 1, the deterministic component and ensemble component are one-way coupled using a consistent spatial resolution for this preliminary investigation. It is used to evaluate the skill of the analyses and forecasts. Initial and

boundary conditions for the deterministic component are obtained by launching a 6-h WRF forecast from a downscaled GFS analysis valid at 1200 UTC. The domain covers exactly the same area as that in the ensemble component. For consistency with the High Resolution Rapid Refresh configuration (HRRR, Smith et al. 2008), the deterministic component chooses the RRTMG scheme for the shortwave and longwave radiation and the MYJ scheme as the PBL scheme during the assimilation cycling, as well as the free forecast period.

Figure 2 illustrates the analysis and forecast cycling set up used in this study. Observations are continuously assimilated from 1800 to 2300 UTC at 15-min intervals for all three events. The analysis variables for driving the WRF Model include wind fields (u, v, w), temperature (T), water vapor mixing ratio (QVAPOR), geopotential height (PH), dry-air mass (MU), and hydrometeor mass (cloud water, rain, ice, snow, graupel), which are updated at each cycle in both the EnKF ensemble and hybrid EnVar deterministic systems. The 3–6-h forecasts are launched every hour beginning at 2000 UTC to provide performance of each experiment during the period of relevant

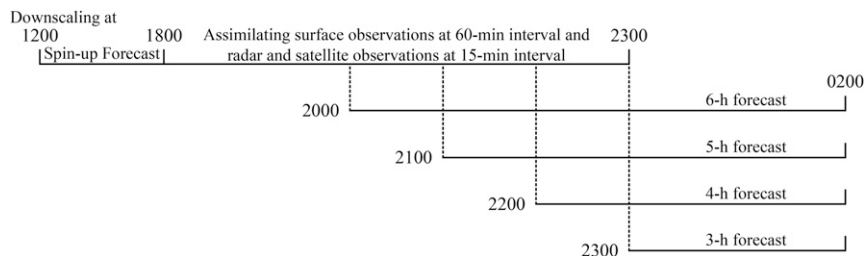


FIG. 2. Flowchart representing assimilation cycles for experiments used by all three high-impact weather events listed in Table 1. Times used in this figure are in UTC.

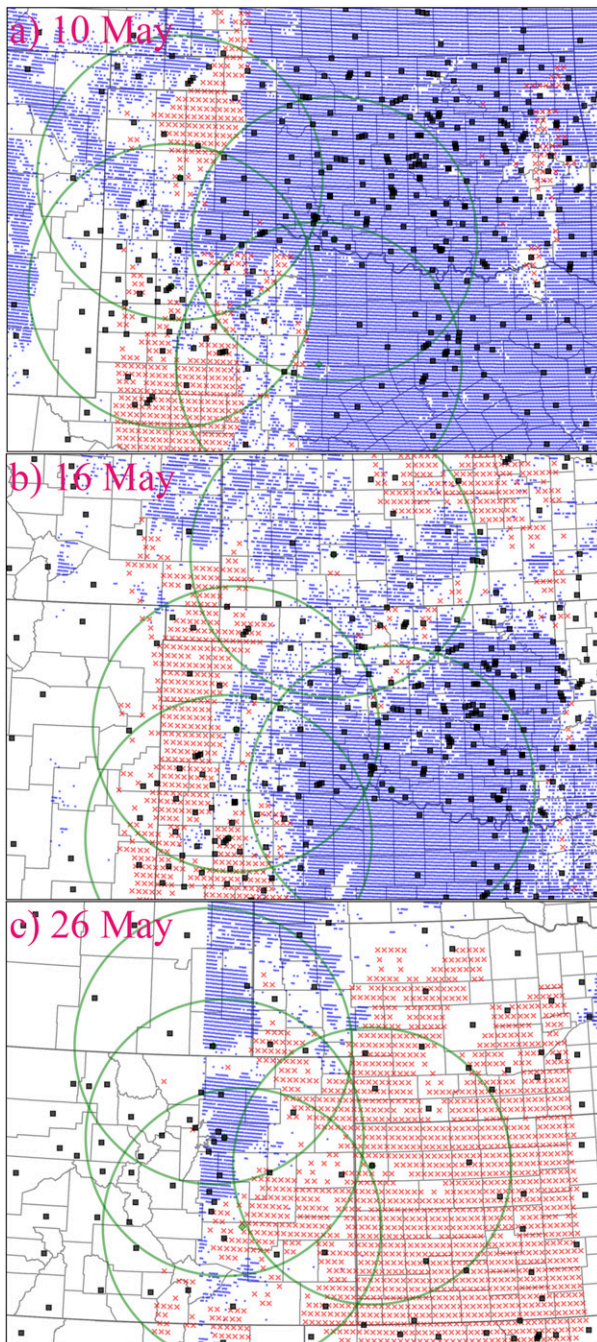


FIG. 3. Locations of the observations assimilated into the hybrid En3DVar system at 1800 UTC for (a) 10, (b) 16, and (c) 26 May 2017 events. Black squares represent surface observations. Green circles represent the coverage of radars. Blue dots and red crosses are the CWP observations in cloudy areas and LPW observations, respectively.

severe weather events. All free forecasts are ended at 0200 UTC on the next day.

Three types of experiments are performed for each event. The control experiment (CTRL) runs without assimilation of

TABLE 3. Observation errors and recursive filter radius used in the variational component of the hybrid 3DEnVar system. The vertical radius of the recursive filter is given in grid points.

Observation type	Error	Horizontal radius (km)	Vertical radius (grid points)
Surface U wind	1.5 m s^{-1}	60	4
Surface V wind	1.5 m s^{-1}		
Surface pressure	2.0 hPa		
Surface temperature	1.5 K		
Surface specific humidity	0.5 g kg^{-1}		
Low-level LPW	0.15 cm		
Midlevel LPW	0.15 cm		
Radial velocity	2.0 m s^{-1}	18	
Reflectivity	10.0 dBZ		
CWP	0.4 kg m^{-2}		

any observations so that it can provide a baseline for comparison between experiments. The second experiment, labeled radar experiment (RAD), assimilates radial velocity, reflectivity, and surface observations. By comparing the above two experiments, the impact of radar and surface observations in convection-allowing NWP can be highlighted. Considering that CWP and LPW observations generally cover different areas (i.e., cloudy area and clear-sky area) and can compensate one another's shortage in coverage (as shown in Fig. 3), the third experiment assimilates both LPW from *GOES-16* and CWP from *GOES-13* in addition to surface and radar observations instead of separately combining CWP or LPW with the radar data, labeled as the radar + satellite experiment (RADSAT). Two additional experiments, one similar to the third experiment but without assimilating LPW (named as RADCWP), and another without assimilating CWP (named as RADLPW) will also be discussed occasionally for the comparison purpose if necessary. Observation errors and recursive filter radius for each type of observation used in the variational system are listed in Table 3. Analyses and forecasts are compared between three types of experiments for each event to investigate whether or not assimilating CWP and/or LPW products has positive impact on analyses and subsequent forecasts.

4. Analysis and forecast results

Since 10, 16, and 26 May 2017 each represent three different synoptic system types, analyses at some particular time when severe weather events were active on these days and their affiliated 3–6-h forecasts are selected for the study. Only the results of the deterministic component of the three experiments are discussed. The subjective diagnostic analyses are provided for each case followed by the qualitative forecast evaluation including comparing the updraft helicity (UH) tracks against SPC storm reports over free forecast periods. To provide a quantitative measure of forecast skill, the frequency bias (BIAS) and fractions skill score (FSS; Roberts and Lean 2008) for composite reflectivity are computed relative to observational data from the Multi-Radar Multi-Sensor system

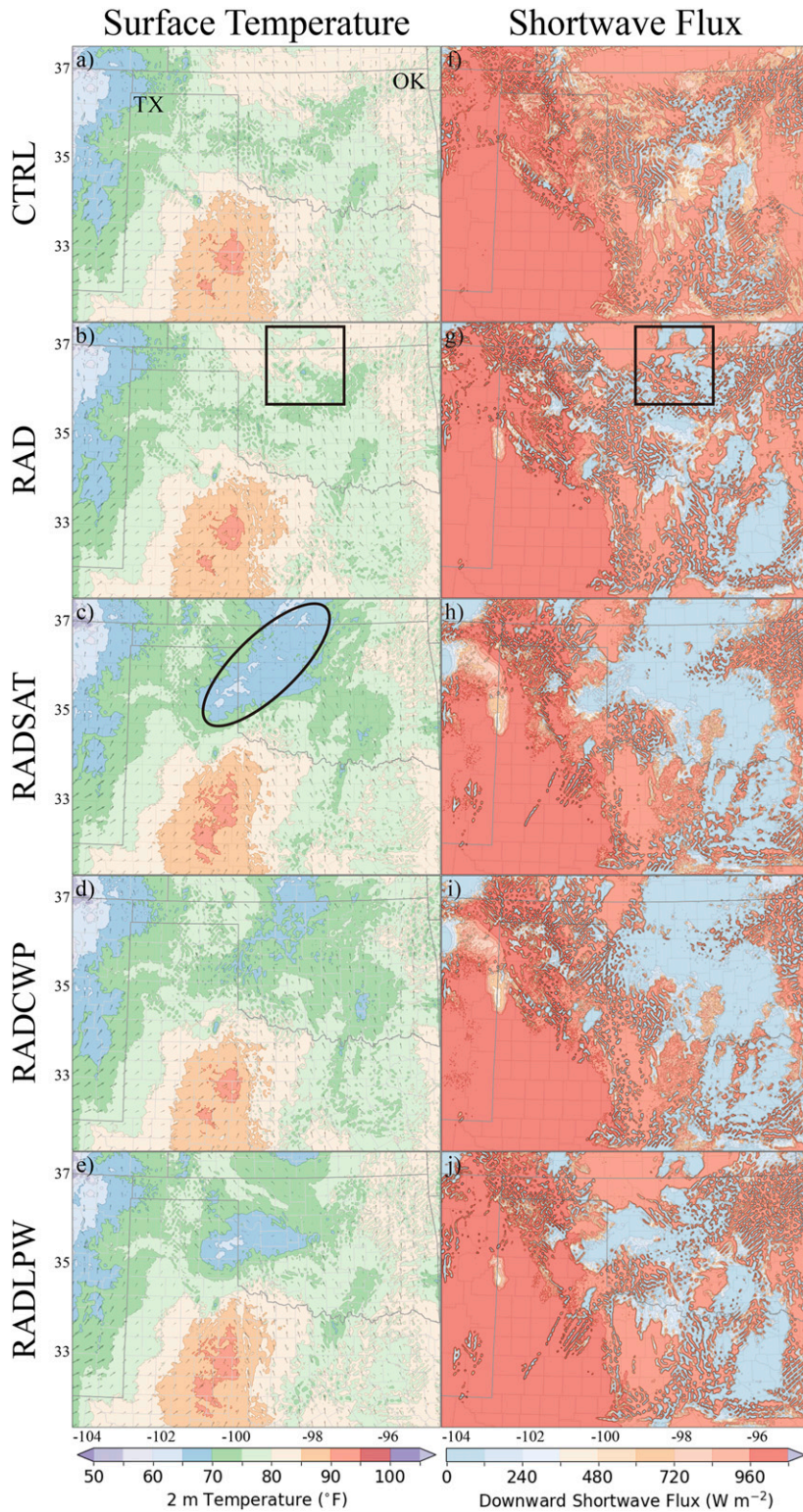


FIG. 4. Analyses of (a)–(e) surface temperature at 2 m above the ground and (f)–(j) downward shortwave flux at surface for CTRL, RAD, RADSAT, RADCWP, and RADLPW experiments at 2000 UTC 10 May 2017.

(MRMS; Smith et al. 2016). Additionally, neighborhood equitable threat scores (ETS; Clark et al. 2010) aggregated over all cases are also calculated relative to NCEP's Stage-IV hourly precipitation product (Baldwin and Mitchell 1997). Finally, information about the statistical metrics and moments of the hybrid En3DVar are given.

a. Analysis diagnostics

1) 10 MAY 2017 CASE

On 10 May 2017, the prestorm environment over Oklahoma and Texas was becoming unstable starting from about 1700 UTC. Near the Oklahoma–Texas border, multiple severe-warned storms, including supercells, developed and affected the area throughout the day (See markers in Fig. 13). Figure 4 shows the surface temperature at 2000 UTC 10 May 2017, after 2 h of data assimilation cycling for each experiment. The temperature gradient along the Oklahoma–Texas border is not sharp or well defined for all experiments (Figs. 4a–e). A slight decrease in temperature ($\sim 5^\circ\text{F}$) is found near the border of the Oklahoma and Kansas in RAD, which is introduced due to the development of storm cells in model (black box, Fig. 4b). In contrast, with the assimilation of satellite-derived observations (Fig. 4c vs Figs. 4a,b), RADSAT generates a large area of cooled surface temperature ($\sim 65^\circ\text{F}$) extending from the eastern part of the Texas Panhandle through northwestern Oklahoma to southern Kansas (ellipse area in Fig. 4c). This pattern agrees with the mesonet observations (ellipse area $\sim 65^\circ\text{F}$ in Fig. 5a; McPherson et al. 2007), which provides a source of independent verification for the analysis. The differences are the consequence of assimilating CWP and LPW observations, which modified the cloud properties in either direct or indirect way. This interpretation is also supported by the standalone RADCWP and RADLPW experiments (Figs. 4d,e).

The downward shortwave flux (SWDOWN in WRF, Figs. 4f–j) represents the amount of downward shortwave radiation reaching the Earth's surface. Higher values of shortwave flux are associated with clear-sky regions and high surface temperatures, while lower values of shortwave flux are associated with the existence of clouds and cooler temperatures. In RAD, the presence of isolated and thick clouds associated with the southern Kansas MCSs is evidenced by low downward shortwave flux values at the same location where the surface temperature is reduced (the green shade in the black box of Fig. 4b, and the blue shade in the black box of Fig. 4g). In the RADSAT experiment, most of Oklahoma and northeastern Texas is associated with low surface temperature and SWDOWN (Figs. 4c,h). This implies extensive cloud cover being present, which is evident on the standalone RADCWP/RADLPW experiments (Figs. 4i,j), and the corresponding *GOES-16* visible image (Fig. 5b). The satellite observations and shortwave flux calculated from the model variables corroborate each other and clearly depict the relationship between the cloud characteristics, downward shortwave radiation and surface temperature. Clouds prevent incoming shortwave solar energy from passing through the atmosphere by reflecting and absorbing shortwave radiation during the daytime, and hence

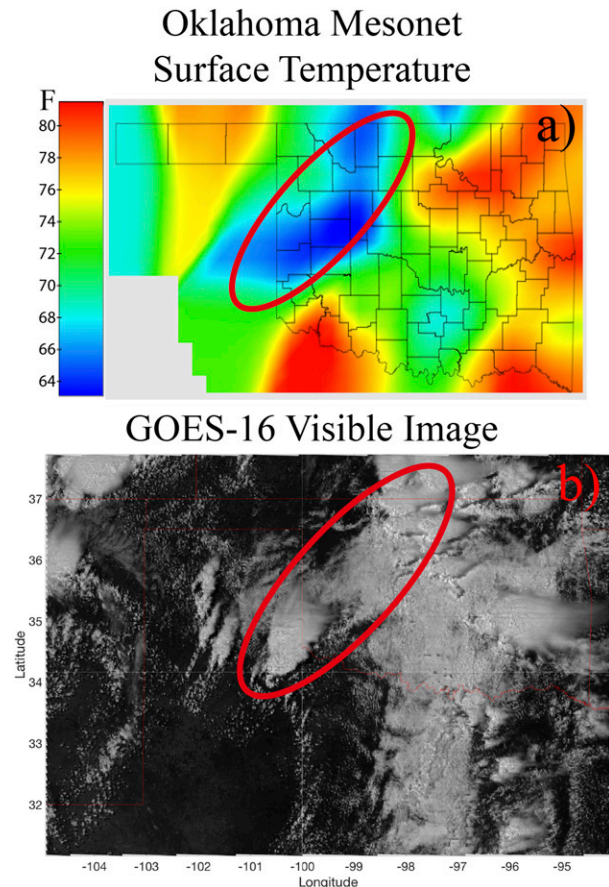


FIG. 5. (a) Mesonet 1.5-m surface temperature and (b) visible image from *GOES-16* at 2000 UTC 10 May 2017.

resist surface heating and lead to a cooler surface. These changes in temperature may further stabilize the lower troposphere and restrain the development of spurious convections in later forecast times.

Water vapor distribution is another critical factor that may affect convective initiation and development. Since the Eq. (1) indicates a linear correlation between the water vapor mixing ratio and simulated model equivalent LPW, the impact of assimilating LPW on water vapor content can be straightforwardly assessed. Differences in water vapor are not obvious between RAD and CTRL at 2000 UTC in most areas (Fig. 6a). The largest difference, $>2 \text{ g kg}^{-1}$, appears near Motley, Texas. The difference is likely due to the ongoing convection. For RADSAT, the difference of water vapor mixing ratio against CTRL reaches as high as 3.0 g kg^{-1} south to the border between Oklahoma and the Texas Panhandle (black box, Fig. 6b). A large area with $>1.5 \text{ g kg}^{-1}$ difference is observed over western Texas (southwest of the model domain) in RADSAT as well. This difference is obviously introduced by assimilating LPW product when we compare RAD against the standalone RADCWP/RADLPW experiments (Fig. 6a vs Figs. 6d,e). The water vapor content in RADSAT increases more than 30% compared to that of RAD [Fig. 6c, RAD has $3\text{--}10 \text{ g kg}^{-1}$ water vapor content over southern Texas Panhandle

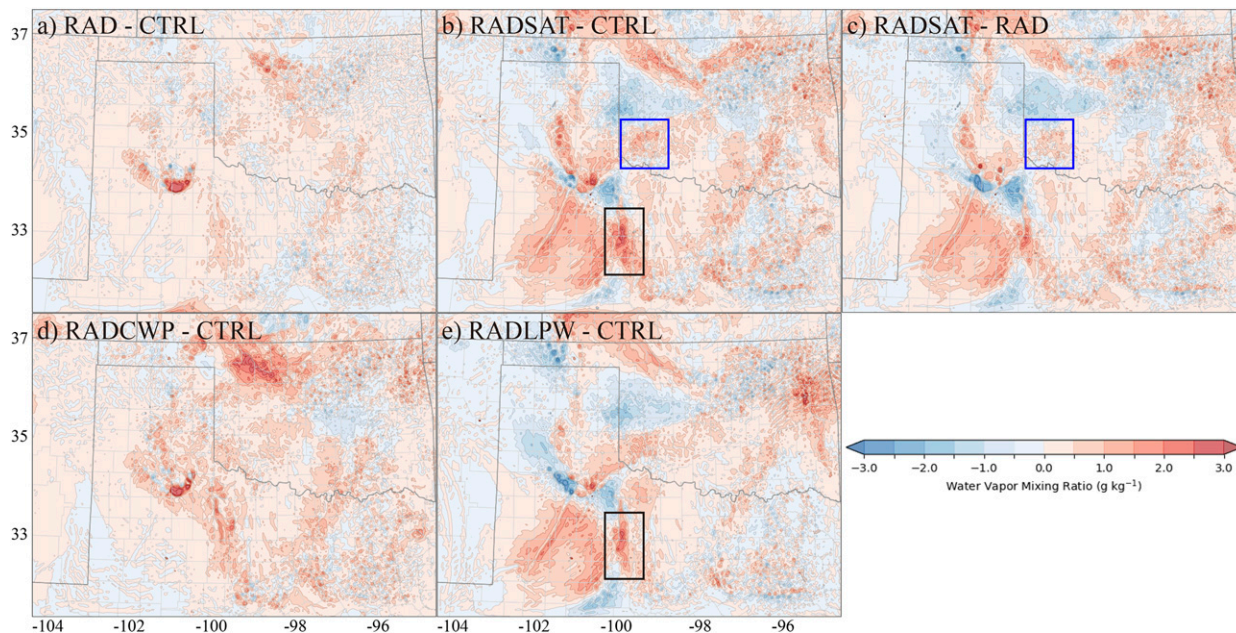


FIG. 6. The differences of analyzed surface water vapor mixing ratio (a) between RAD and CTRL, (b) between RADSAT and CTRL, (c) between RADSAT and RAD, (d) between RADCWP and CTRL, and (e) between RADLPW and CTRL at 2000 UTC 10 May 2017. The black box highlights one of differences of water vapor mixing ratio between RADSAT/RADLPW and CTRL. The blue box highlights one of differences of water vapor mixing ratio between RADSAT and CTRL/RAD.

(not shown)], which may lead to a more favorable moisture content for initiating deep moist convection when accompanied with a strong lifting process. In addition, an area with positive differences in water vapor is observed over southwestern Oklahoma when comparing RADSAT and CTRL/RAD (blue boxes in Figs. 6b,c). In summary, a more reasonable water vapor mixing ratio field is able to either benefit the suppression of spurious convection or to promote new cell developments for this case.

Comprehensive changes of model's thermodynamic conditions can be evaluated by the mixed layer convective inhibition (MLCIN) and mixed layer convective available potential energy (MLCAPE) (Fig. 7). Essentially, high MLCIN occurs in areas of cool surface temperatures caused by clouds and precipitation. Both CTRL and RAD produce a high MLCIN over southeastern Oklahoma and eastern Texas. Differences in MLCIN between CTRL and RAD (Figs. 7a,b) are evident over southern Kansas. RADSAT also generates high MLCINs over southeastern Oklahoma and eastern Texas. But apparently, it also generates high MLCINs in southern Kansas, northwestern Oklahoma and eastern Texas Panhandle (Fig. 7c), and low MLCAPEs near the same areas (Fig. 7f). The cloud cover with $CWP > 1.5 \text{ kg m}^{-2}$ (ellipse area in Fig. 5b and corresponding area in Fig. 4h) allows stabilization of the low-level atmosphere and $MLCIN < -200 \text{ J kg}^{-1}$ for the same reason. Compared to the CTRL experiment, RAD does not significantly change the MLCAPE at 2000 UTC (Figs. 7d,e). In contrast, the MLCAPE over the clear-sky area in southwestern Oklahoma increases to around 2750 J kg^{-1} in RADSAT. This increase corresponds well with the difference of water vapor mixing ratio at surface

(Figs. 6b,c). Consequently, a supercell that produced several tornadoes developed at a later time.

2) 16 MAY 2017 CASE

The 16 May 2017 event was characterized by the presence of a dryline that extended southward from western Kansas down to the U.S.–Mexico border at 1800 UTC. Storms formed at the intersection of the dryline and weak frontal boundary zonally crossing central Kansas (https://www.wpc.ncep.noaa.gov/archives/web_pages/sfc/sfc_archive_maps.php?arcdate=05/16/2017&selmap=2017051621&mapttype=namussfc). From 1800 to 2100 UTC, the dryline remained stationary and convection initiated at several locations ahead of the dryline. Similar to the 10 May 2017 event, the differences between three experiments for surface water vapor mixing ratio are analyzed (2100 UTC). A narrow band of negative differences exceeding 3 g kg^{-1} is observed in the middle of the Texas Panhandle in the of moisture difference field between RAD and CTRL (Fig. 8a). The difference between RADSAT and CTRL is quite similar to that between RAD and CTRL, but positive differences $> 3 \text{ g kg}^{-1}$ are also present over the southern Texas Panhandle (black box, Fig. 8b). Farther south, the difference becomes negative between RADSAT and CTRL, and between RADSAT and RAD (Figs. 8b,c). Moreover, RADSAT generates a positive difference in surface moisture ahead of the dryline along the border of the eastern Texas Panhandle and western Oklahoma. These changes promote a bulge of dry air toward the moist air to the east, intensifying the moisture gradient over this area in RADSAT.

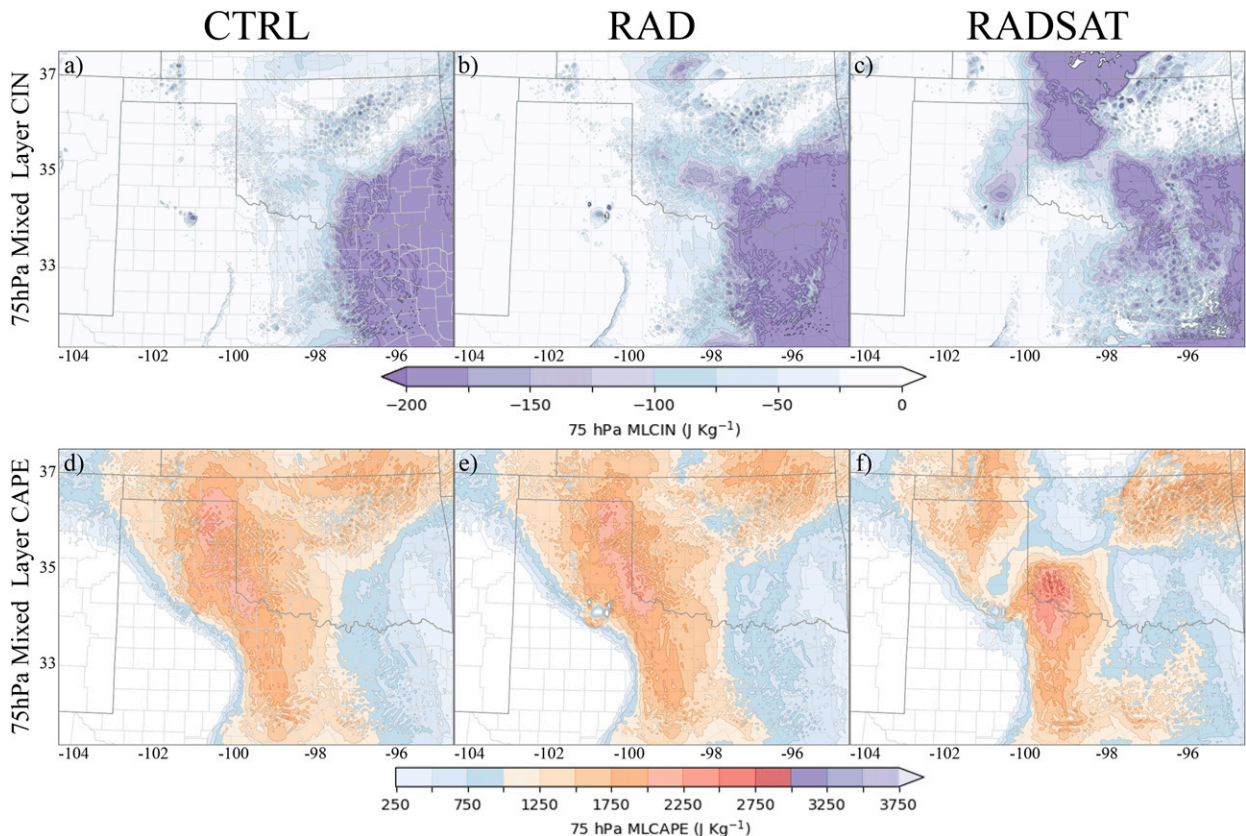


FIG. 7. (a)–(c) The lowest 75-hPa mixed-layer convective inhibition (MLCIN) and (d)–(f) the lowest 75-hPa mixed-layer convective available potential energy (MLCAPE) for CTRL, RAD, and RADSAT experiments at 2000 UTC 10 May 2017.

3) 26 MAY 2017 CASE

The third analyzed event occurred on 26 May 2017 in Colorado. Based on the sounding (KDNR, not shown) at 0000 UTC 27 May 2017, this event is characterized by low an inertial instability and high vertical wind shear environment. Figure 9 exhibits differences of surface water vapor mixing ratio in the analyses between experiments. RAD produces more water vapor ($>1 \text{ g kg}^{-1}$) over southeast Wyoming and in northeastern Colorado, which is near the tornadic supercell (black box, Fig. 9a). RADSAT appears to reduce water vapor ($<-1 \text{ g kg}^{-1}$) over the area southeast to the tornadic supercell, but slightly increases the water vapor ($>0.5 \text{ g kg}^{-1}$) in northeastern Colorado and northwestern Kansas (Figs. 9b,c). More apparent differences are observed in the intensity of vertical wind shear, which is one of the most important factors that may affect the accuracy of predicting convection (Weisman and Klemp 1982). All experiments generate 0–1-km vertical wind shear greater than 20 m s^{-1} , which is associated with the soon-to-be-tornadic convection in northeastern Colorado (Figs. 9d–f). Both RAD and RADSAT intensify the vertical wind shear in northeastern Colorado (red boxes) while RADSAT also changes the pattern of vertical wind shear in southeastern Wyoming (Blue boxes) compared to CTRL and RAD experiments.

4) GENERAL DISCUSSIONS OF REFLECTIVITY FOR ALL THREE CASES

Some differences in the analyzed composite reflectivity are shown among the experiments depending on what kind of observations are assimilated. For the 10 May 2017 event (Fig. 10), CTRL misses the supercell located in the southern Texas Panhandle at 2000 UTC, but also produces spurious cells farther south when compared with MRMS data (Fig. 10a vs Fig. 10b). RAD analyzes the major supercell (Storm 1) but misses the storm cells in southeastern Oklahoma (Fig. 10a vs Fig. 10c). Only RADSAT correctly places all storms near or at their observed locations, especially for the major supercell over the Texas Panhandle, which produces several tornadoes at later times in the forecast near the Red River in addition to producing more storm cells near the border of Oklahoma and Kansas (Fig. 10a vs Fig. 10d) though small spurious cells exist.

For the 16 May 2017 event (Fig. 11), CTRL produces both storm 1 and storm 2 over the Texas Panhandle at 2100 UTC, which match the MRMS data (Fig. 11a vs Fig. 11b). But the storm cluster over southwestern Kansas has significant phase errors. The pattern of the cluster prefers a southwest–northeast orientation as shown in MRMS data rather than a south–north orientation in CTRL. The pattern is somewhat corrected in RAD, but more areas over southwestern Kansas are covered

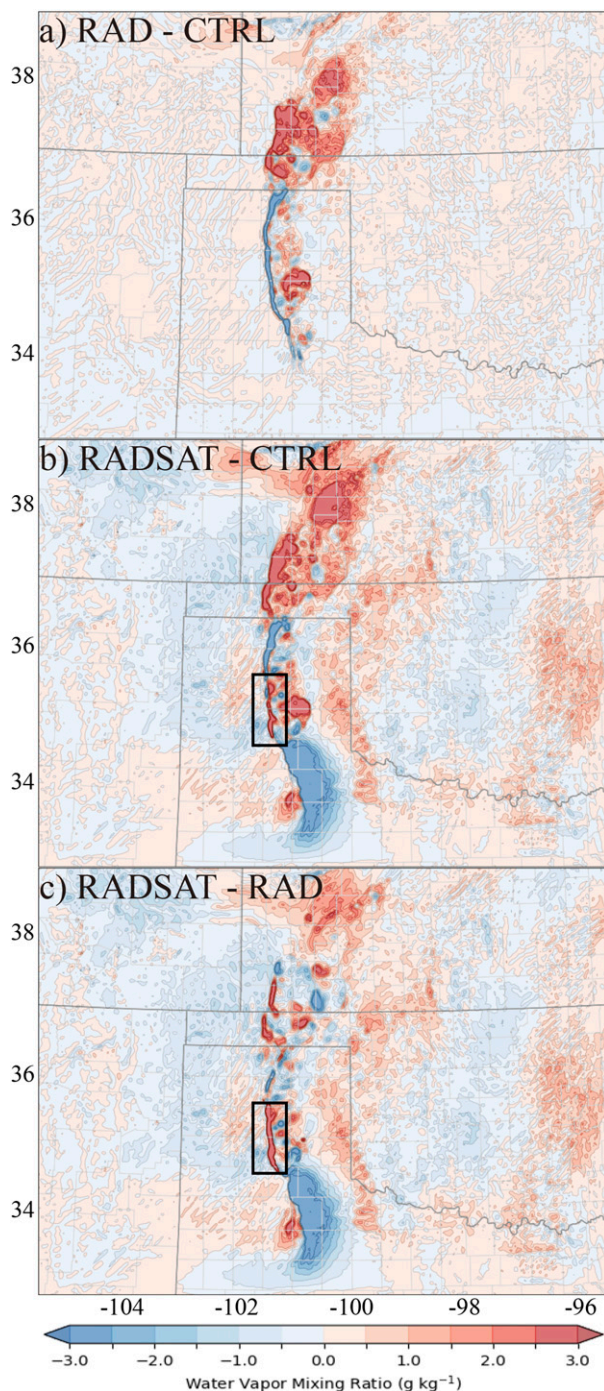


FIG. 8. As in Fig. 6, but at 2100 UTC 16 May 2017. The black box indicates the positive difference between RADSAT and CTRL/RAD.

by simulated composite reflectivity > 40 dBZ compared to the MRMS data (Fig. 11a vs Fig. 11c). In RADSAT, the intensity (in dBZ) of the cluster seems match the observations well, but also produces spurious cells around this area (Fig. 11a vs Fig. 11d).

For the 26 May 2017 event (Fig. 12), both CTRL and RAD produce a strong supercell at southeastern Colorado at 2100 UTC, which is not seen in the MRMS data (Fig. 12a vs Figs. 12b,c), while RADSAT only generates a much weaker small-scale spurious cell at the same location (Fig. 12d). Moreover, less spurious cells with > 40 dBZ composite reflectivity are observed over southeastern Wyoming and southeastern Colorado in the RADSAT experiment.

b. Qualitative forecast evaluation

For the first 2-h forecasts of the 10 May event, all experiments generate the supercell in the Texas Panhandle near the southwest corner of the Oklahoma, but many spurious cells exist in both CTRL and RAD in the north Texas Panhandle and Oklahoma Panhandle indicating large overprediction of convection (Figs. 10f,g,j,k). RADSAT has the best prediction of the storms in general (Figs. 10h,l) likely because the assimilation of satellite-derived data weakens the spurious convection in these areas. In the next 3-h forecasts, this issue has been slightly alleviated but still exists in both CTRL and RAD. Moreover, large phase errors for the storm cluster around the south west corner of Oklahoma are observed in both CTRL and RAD (Figs. 10n,o,r,s,v,w). The storms in CTRL and RAD exhibit north biases compared to the MRMS data. The relative locations of the storms in CTRL prefer a south–north orientation instead of a southwest–northeast orientation as shown in the MRMS data. RADSAT performs better, especially for the orientation and location of the storms that produced tornadoes along the Red River (Figs. 10p,t,x). The improvements observed in RADSAT are probably the consequence of combining changes in water vapor distribution over southwestern Oklahoma and its associated impact on MLCAPE and MLCIN, which are primarily due to the assimilation of LPW observations.

For the 16 May event, the result of 3-h forecast launched from 2100 UTC corresponds well to the analyses previously discussed. Two separate tornadic supercells are predicted by all three experiments between 2100 and 0000 UTC (Figs. 11a–p). However, two important improvements are present in RADSAT. The 1- and 2-h forecasts for composite reflectivity show that all experiments maintain an MCS in western Kansas, while RADSAT generates an MCS pattern (Fig. 11h) slightly closer to the observations at 2200 UTC (Fig. 11e) though many small spurious cells exist. The MCS appears as a southwest–northeast linear shape at 2300 UTC in RADSAT (Fig. 11i), which is similar to observed composite reflectivity (Fig. 11i) compared to CTRL and RAD. Another improvement is related to the predictability of storm 3 (Fig. 11i). Only RADSAT produces a better forecast by generating this nontornadic supercell associated with large hail damage while both CTRL and RAD fail to generate an isolated supercell in this region.

An improved forecast of severe convection on 26 May is also observed by comparing the simulated composite reflectivity within 3-h forecasts launched from 2100 UTC (Figs. 12a–p). All three experiments appropriately predict the tornadic supercell in northeastern Colorado during the 3-h forecast period. CTRL differ from RAD and RADSAT in that it produces the

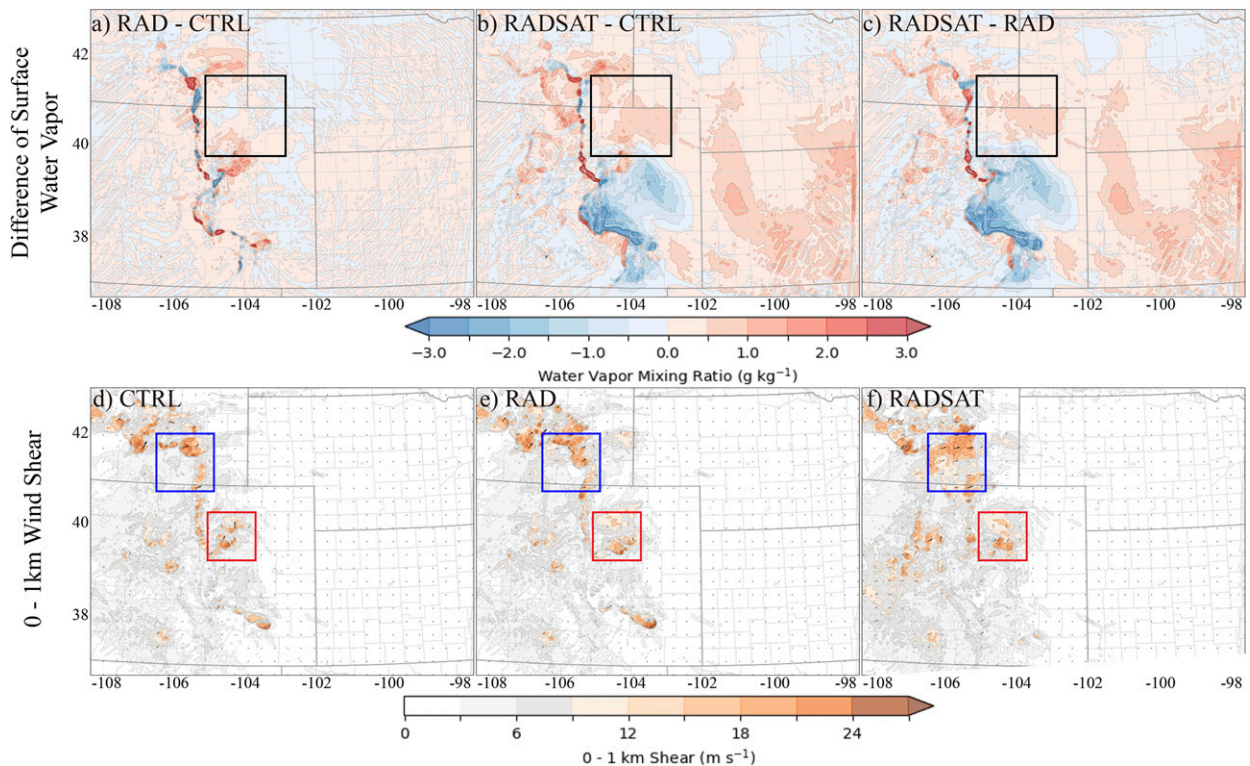


FIG. 9. (a)–(c) The differences of analyzed water vapor mixing at the surface between experiments, as well as (d)–(f) 0–1-km wind shear for (d) CTRL, RAD, and RADSAT, respectively, at 2100 UTC 26 May 2017.

tornadic supercell falling behind the location observed in the MRMS data. For example, RAD and RADSAT (Figs. 12k,l) produce the tornadic supercell at Washington county, Colorado, as in the MRMS observation (Fig. 12i), while CTRL produce the tornadic supercell at Arapahoe county, Colorado. At 2200 UTC, 1 h into the forecast, although RADSAT overpredicts the storm initiated in the southeast corner of Wyoming (Fig. 12e vs Fig. 12h), and the other two experiments totally miss this storm (Figs. 12f,g). At 2300 and 0000 UTC, RADSAT maintains the storm similar to that in the MRMS observations. However, it produces more spurious cells near the border of Colorado and Kansas (Figs. 12l,p) compared to the CTRL (Figs. 12j,n) and RAD (Figs. 12k,o).

To illustrate the motion of convection associated with severe weather events, the 2–5-km UH tracks for 6-h forecasts launched from 2000 UTC 10 May (Fig. 13), 2100 UTC 16 May (Fig. 14), and 2100 UTC 26 May (Fig. 15) are overlaid with the NWS local storm reports recorded by the Storm Prediction Center (SPC) during these time periods. The larger updraft helicity represents the stronger vertical motion and midlevel rotation between 2 and 5 km at a given horizontal grid point.

On 10 May 2017, each experiment generates a UH track along or north of the reported severe storm events near the border of southwestern Oklahoma and north Texas. A hysteresis of strong UH associated with the storm 1 (indicated in Fig. 10e) is predicted although it is imbedded in spurious convections in CTRL (Fig. 13a). RADSAT best matches the

track and intensity of UH to the NWS reports not only for the first storm, but also for the second storm observed around 2300 UTC in Foard County, Texas (Fig. 10m). By comparing RADSAT and the standalone RADCWP/RADLPW experiments (Fig. 13c vs Figs. 13d,e), it is apparent that the improvement in initial conditions, and hence convection initiation and the movement of convection is due to the assimilation of LPW product.

For the 16 May event, all experiments produce similar 2–5-km UH tracks and intensities ($>450 \text{ m}^2 \text{ s}^{-2}$) for the tornadic supercells. RADSAT generates a UH track almost exactly matching the NWS reports for both tornadic supercells and nontornadic supercell (Figs. 14c, 11i), whereas CTRL and RAD totally miss the third storm (Figs. 14a,b). RADSAT also provides a somewhat better UH track forecast for the hazardous weather events including tornadoes in southwestern Kansas between 2100 and 0000 UTC.

As expected, all experiments for 26 May generate a UH track with value greater than $450 \text{ m}^2 \text{ s}^{-2}$ for the tornadic supercell. However, CTRL has a south bias compared to the SPC reports (Fig. 15a). Both RAD and RADSAT generate tracks better overlapping the SPC reports. Although RADSAT has lower UH values along the track, it highlights the southeastern turn that occurred with the storm just after the first tornado formed (Fig. 15c). Apparently, the storm in RADSAT is moving along the path where larger moisture gradient is observed (Figs. 9b,c). Therefore, the differences of forecasts

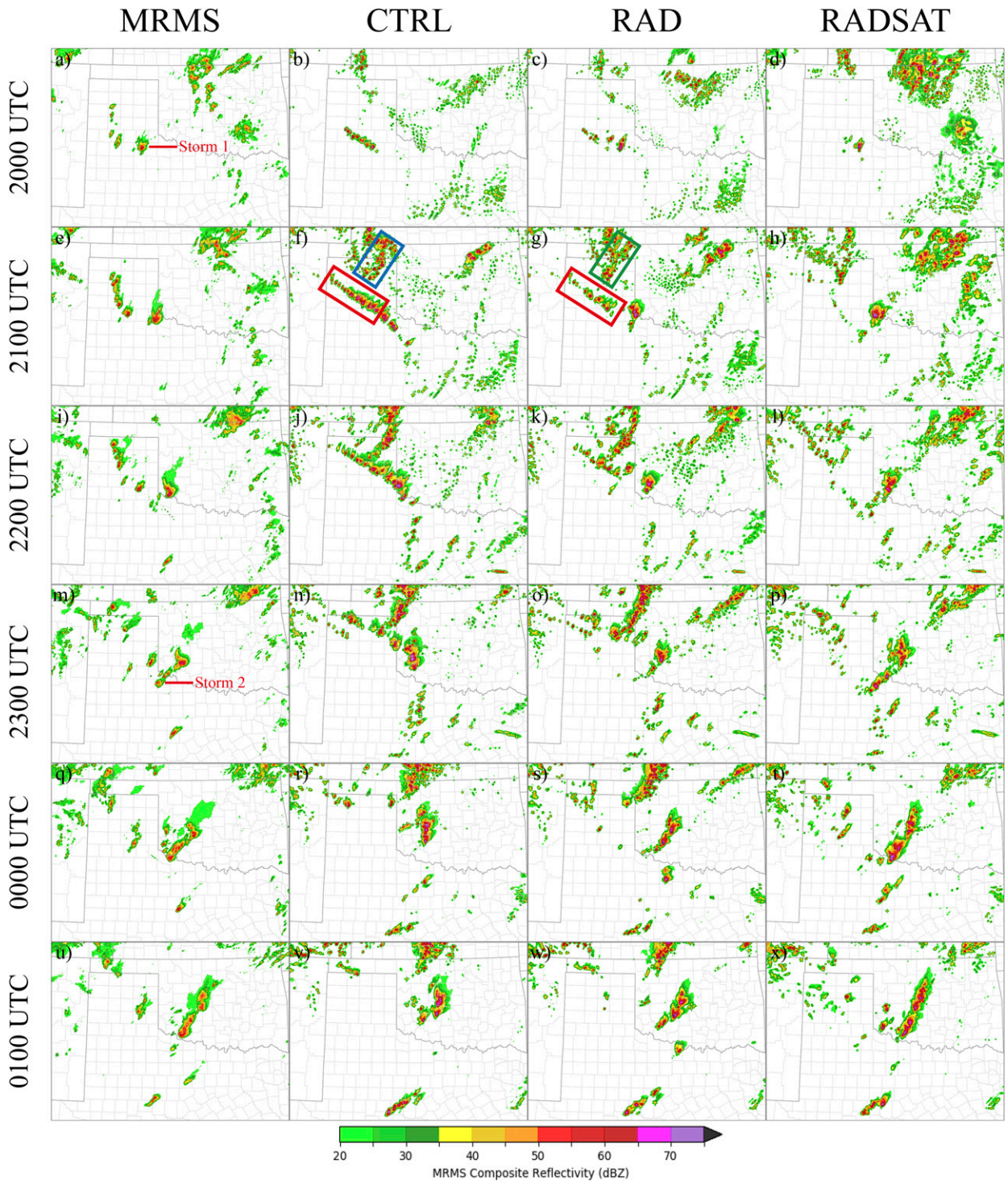


FIG. 10. (from left to right) The composite reflectivity from MRMS and the forecasted composite reflectivity for CTRL, RAD, and RADSAT. (a)–(d) The analysis at 2000 UTC 10 May 2017. The (e)–(h) 1-, (i)–(l) 2-, (m)–(p) 3-, (q)–(t) 4-, and (u)–(x) 5-h forecasts initiated at 2000 UTC. Boxes in (f) and (g) indicate the locations of overprediction without using satellite observations during the assimilation cycles.

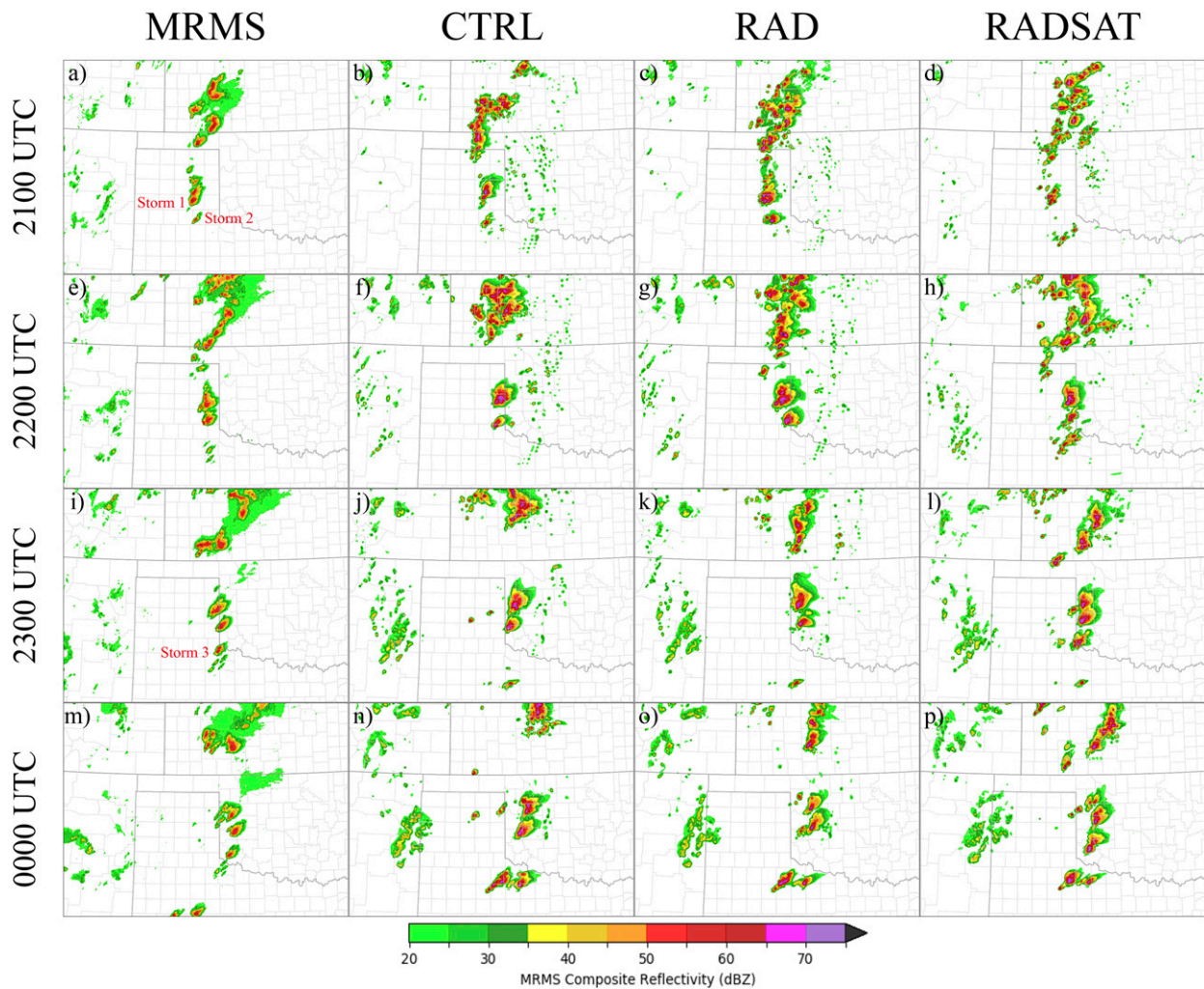


FIG. 11. As in Fig. 10, but for 3-h forecasts initiated at 2100 UTC 16 May 2017.

between the RADSAT and other experiments are very likely related to the changes in water vapor distribution related to the assimilation of LPW.

c. Quantitative forecast evaluation

Although the subjective comparisons of composite reflectivity and UH track between the experiments suggest that assimilating additional satellite observations improves the skill of convection forecasts, the quantitative verification is essential to objectively assess the impact of assimilating different observations on the short-term forecasts. First, the simulated composite reflectivity and hourly accumulated precipitation are interpolated from model space to observation space by applying bilinear interpolation in horizontal and linear interpolation in vertical. Then, the BIAS and FSS of composite reflectivity and ETS of hourly accumulated precipitation are calculated relative to the MRMS composite reflectivity and the NCEP Stage-IV product (Lin and Mitchell 2005), respectively. Composite reflectivity uses 20 and 40 dBZ as thresholds to assess the performance of each experiment, while hourly

accumulated precipitation uses 2- and 10-mm thresholds. The neighborhood radius of 12 km is chosen for all these score calculations. The results are aggregated over 3-h forecasts initiated every 1 h between 2000 and 2300 UTC for all three cases (see Fig. 2). For the FSS and ETS, a value of 1.0 indicates a perfect forecast and the value of zero indicates no forecast skill. A bias of 1.0 indicates no bias, whereas values over 1.0 indicate overprediction and values below 1.0 indicate underprediction.

Using 20 dBZ as a threshold for reflectivity, the biases are generally small (close to 1.0) during most of 3-h forecast period for all three experiments (Fig. 16a). However, positive biases exist during the early stage of the forecasts for both RAD and RADSAT experiments. This is due to the initiation of spurious cells at early forecast time and they disappear along with the forecast time moving forward. For the 40-dBZ threshold, the results are different (Fig. 16b). All experiments have bias scores greater than 1.0, indicating general overpredictions throughout the entire forecast period. The RADSAT maintains ~ 0.2 lower BIAS scores compared to the RAD and CTRL.

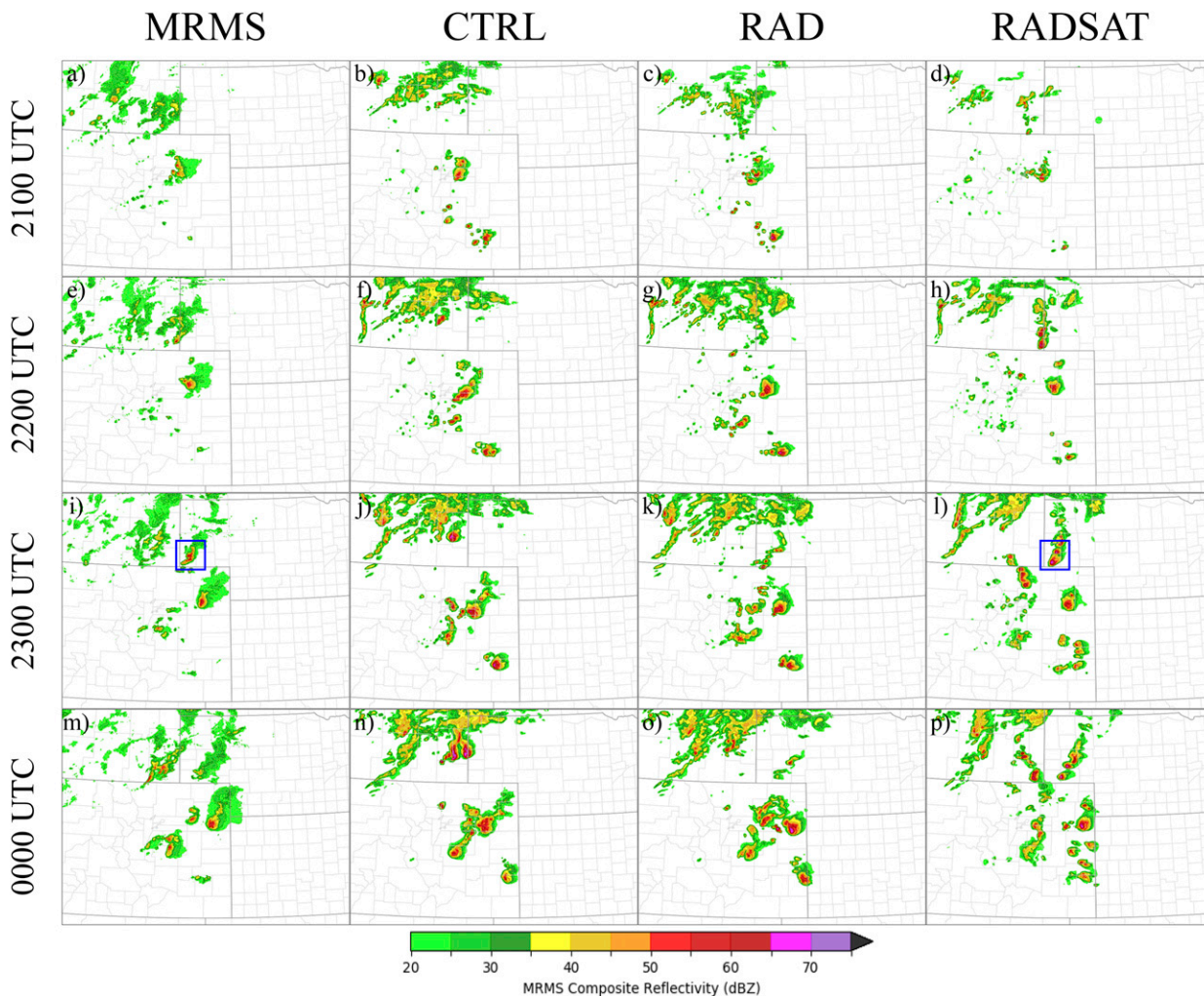


FIG. 12. As in Fig. 10, but for 3-h forecasts initiated at 2100 UTC 26 May 2017.

The FSS of RADSAT is always better than the other two experiments for both thresholds (Figs. 16c,d) during the forecast period. Unlike the CTRL experiment, which produces almost constant lowest performance in term of the FSS, RAD, and RADSAT initially have higher scores (between ~ 0.4 and ~ 0.7) and decrease gradually as a function of forecast lead time. At the end of the 3-h forecast period, the FSS of RADSAT is approximately 0.1 higher than that of CTRL and 0.05 higher than that of RAD for both thresholds. Overall, RADSAT outperforms other two experiments, and RAD outperforms CTRL against MRMS composite reflectivity.

The 1-h accumulated precipitation performance relative to the Stage-IV hourly precipitation product tells a similar story. For the 2-mm threshold, RADSAT outperforms 1-h accumulated precipitation by 0.05 and 0.1 compared to RAD and CTRL, respectively (Fig. 16e). It is worth noting that the performance of the first hour precipitation forecast in RADSAT is slightly degraded and about 0.14 lower than the RAD

experiment. This overall improvement is further supported with the verification using a 10 mm threshold (Fig. 16f). In general, the skill of 1-h accumulated precipitation forecasts for all experiments decreases with time except CTRL experiment with 10-mm threshold.

d. Hybrid En3DVar statistical metrics analysis

To assess the quality of the hybrid En3DVar analysis cycling, some features of statistic metrics including the behavior of the normalized total functions, mean (bias), and root-mean-square (rms) for innovation and analysis residual during the cycling period are discussed. These metrics were defined in detail by Fierro et al. (2019). During the minimization process of the hybrid En3DVar, the values of the cost function for each observation type generally decrease as a function of iteration number. It is also convenient to measure the distance between the observations and the background fields or the analysis by analyzing the rms innovation and the rms residual by applying the following equations (Fierro et al. 2019):

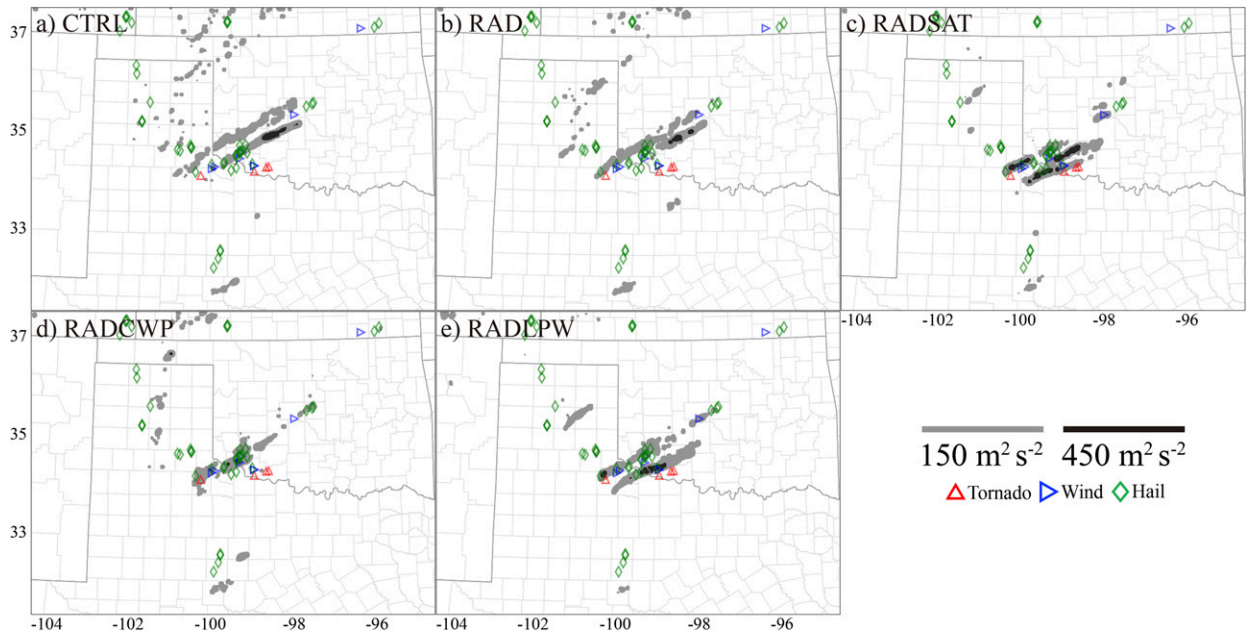


FIG. 13. The tracks of UH between 2 and 5 km above ground (shaded) drawn from 6-h forecasts initiated at 2000 UTC 10 May 2017 for the (a) CTRL, (b) RAD, (c) RADSAT, (d) RADCWP, and (e) RADLPW experiments. The red, blue, and green markers indicate reports of tornadoes, damaging wind, and large hail, respectively.

$$\text{RMS_Innov} = \sqrt{\frac{1}{N} \sum_{i=1}^N [y_i - H(x_i^b)]^2}, \quad (4)$$

$$\text{RMS_Res} = \sqrt{\frac{1}{N} \sum_{i=1}^N [y_i - H(x_i^a)]^2}, \quad (5)$$

where N is the number of observations, y is the observation, and $H(x)$ is forward operators transferring the background fields (x^b) or the analysis field (x^a) from model space to observation space. Moreover, the mean innovation and mean analysis residual are analyzed to determine if any biases are generated for control variables by the data assimilation process:

$$\text{Mean_Innov} = \frac{1}{N} \sum_{i=1}^N [y_i - H(x_i^b)], \quad (6)$$

$$\text{Mean_Res} = \frac{1}{N} \sum_{i=1}^N [y_i - H(x_i^a)]. \quad (7)$$

Because the results of all three cases are qualitatively similar, only the first event (10 May 2017) is discussed.

In general, both RAD and RADSAT experiments show a decrease in the total cost function with the RAD experiment at various analysis times producing a reduction ranging between 50% and 80% at the end of the minimization process. The largest decrease (over 75%) is observed at initial analysis time 1800 UTC (Fig. 17a). Given more observations being assimilated, RADSAT generally has 10% less reduction compared to RAD at the same analysis time (Fig. 17b). RAD produces greater reduction (around 40%) of the total cost function at the

first three iterations at 1800 and 1900 UTC, while the RAD experiment for the remaining analysis times and the RADSAT experiment for all analysis times have stable reduction rates between iterations.

The innovation biases for LPW are positive and largely depart from the reference line (exceeding 1 mm) for the first 30 min of the data assimilation cycling (Fig. 17d), indicating that the background fields initially have dry biases compared to the observations over most part of the domain; especially over western Texas and southwestern Kansas (Fig. 6). Since the dry biases are ameliorated within 3 analysis timestamps by assimilating LPW observations, the innovation and analysis residual biases for LPW fluctuate around the reference line starting from 1830 UTC. The innovations for radial velocity have negative biases between 1800 and 2000 UTC, but both innovation and residual for radial velocity turn to be identical and close to zero since 2000 UTC for both RAD and RADSAT experiment (Figs. 17c,d). This indicates that the analyzed radial velocity fields fit the observations very well. For reflectivity, the innovations are positive with largest bias ~ 13 dBZ at 1800 UTC and decreasing at later data assimilation cycles. They finally alter to be negative since 2100 UTC and reach lowest value (~ -5 to -6 dBZ) near 2145 UTC. In contrast, the residuals for reflectivity are close to the reference line only between 1800 and 1900 UTC for RAD and between 1800 and 2000 UTC for RADSAT. Over the whole data assimilation cycling period, they are consistently negatively biased. This statistical feature suggests that the non-linearity of reflectivity forward operators may prevent the data assimilation system from readily absorbing all the information from reflectivity observations. The rms statistics

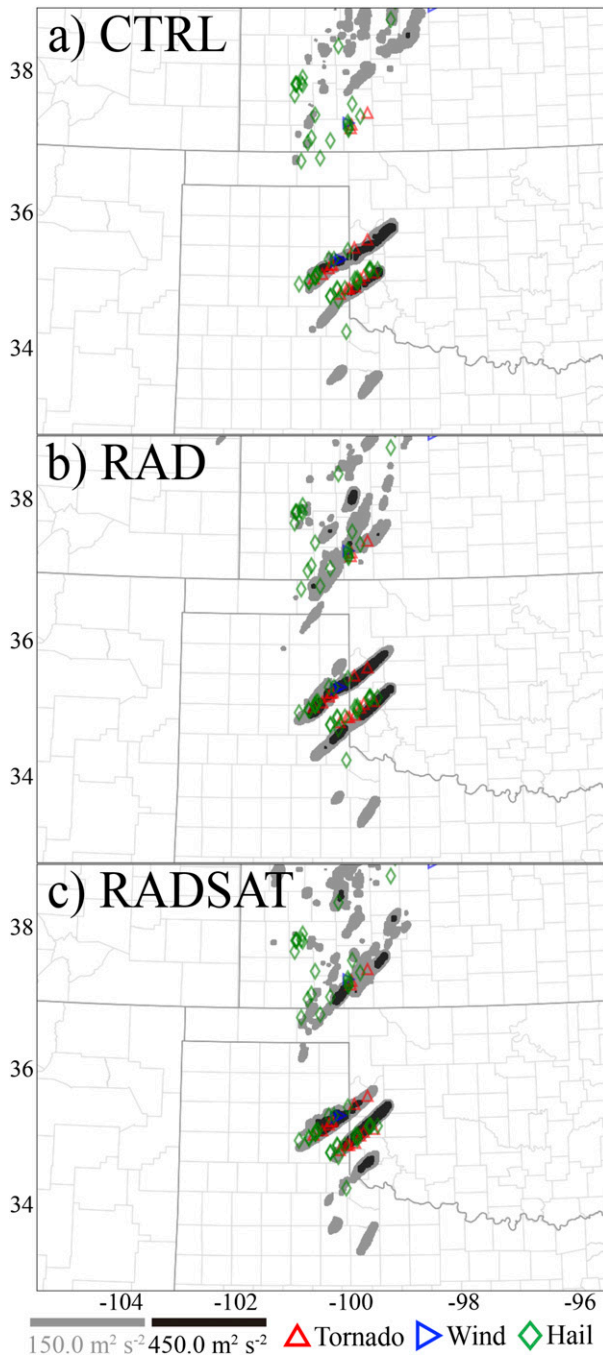


FIG. 14. As in Fig. 13, but for 3-h forecast initiated at 2100 UTC 16 May 2017.

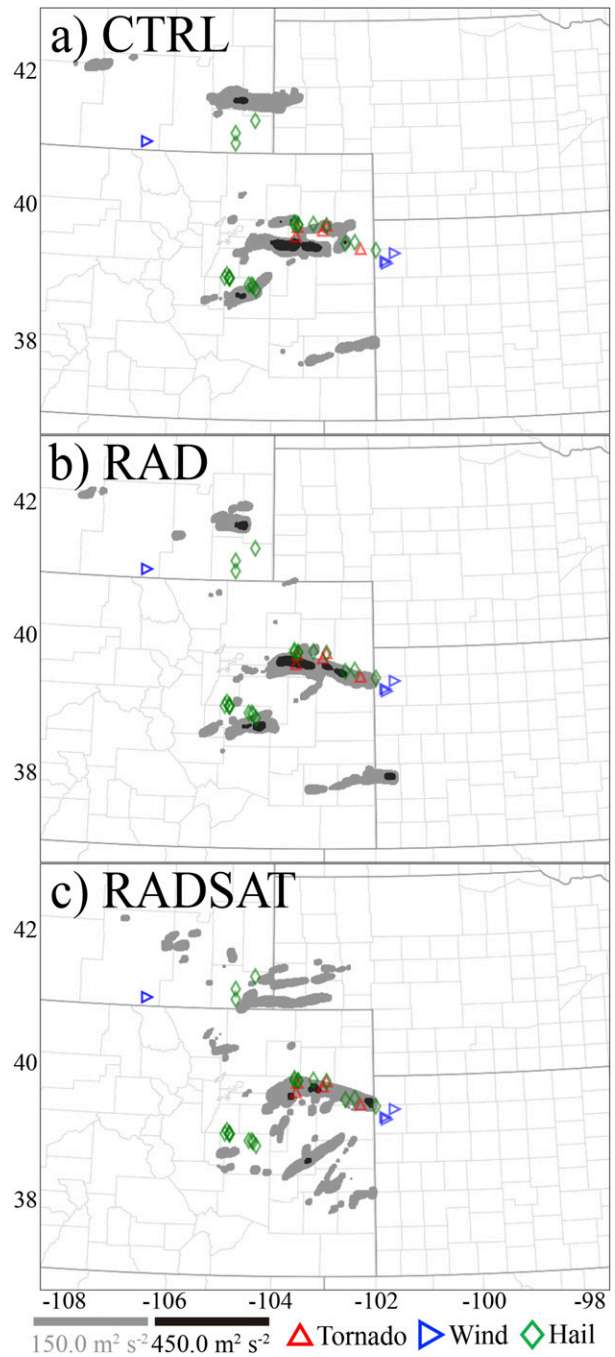


FIG. 15. As in Fig. 13, but for 4-h forecast initiated at 2100 UTC 26 May 2017.

(Figs. 17e,f) show that the values for analysis residual are typically smaller than the innovation values. The analysis is able to reasonably fit all kinds of observations during the whole cycling period. Moreover, the residual values for all types of observations are close to their corresponding observation errors, respectively, indicating these observations are properly assimilated.

5. Conclusions and future work

In this research, three experiments are conducted to investigate the impact of assimilating radar, surface, and satellite retrieved CWP and LPW observations on short-term convective-scale NWP with three HIWeather events that occurred in May 2017. The CTRL experiment does not assimilate any observations. The RAD experiment assimilates radar and

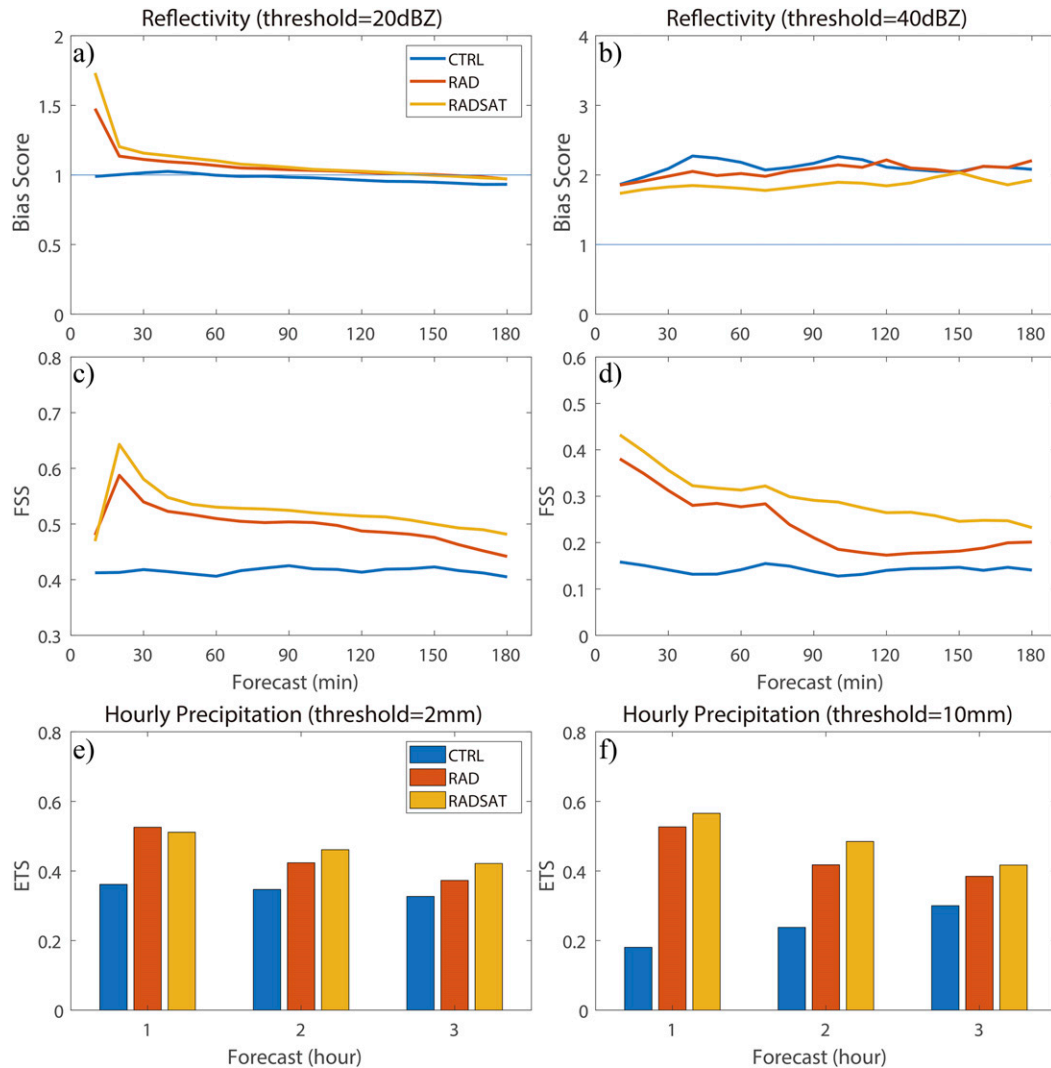


FIG. 16. (a),(b) Frequency bias and (c),(d) fractions skill score (FSS) of composite reflectivity forecasts against the MRMS observations over the simulation domain. The thresholds used for verification are 20 and 40 dBZ. The results aggregate 3-h forecasts starting from 2000, 2100, 2200, and 2300 UTC of all three events. (e)–(f) Bars indicate ETS of hourly accumulated precipitation against the NCEP Stage-IV product aggregated over the same time period, but using 2 and 10 mm as a threshold.

surface observations, and the RADSAT experiment further assimilates satellite derived CWP and LPW products in addition to the radar and surface data. Generally, the comparison of results from three types of experiments indicates the improvement on model initial conditions and short-range forecasts for three severe weather events when CWP and/or LPW are also assimilated in addition to radar and surface data.

For the 10 May 2017 event, assimilating CWP improves the cloud property analysis, the downward shortwave radiation over the cloudy areas, and therefore surface temperature and atmospheric instability. Spurious cells are mostly removed in later forecasts due to this improvement. Assimilating the LPW product also yields positive results for CI by saturating

the moisture fields surrounding the ongoing convection. The improved analysis typically generates high UH swaths that are more appropriately placed when compared against the SPC damage reports.

Similar impacts of assimilating satellite products are observed for the other two cases. For the 16 May 2017, RADSAT leads to intensified moisture gradient at the surface compared to CTRL and RAD. As a result, the storms of interest are better analyzed and predicted when verified against the observations. For the 26 May 2017, RADSAT improves water vapor distribution at the surface and low-level vertical wind shear, leading to better placed storms in the model at times and locations consistent with the observations. Again, the reflectivity and UH track

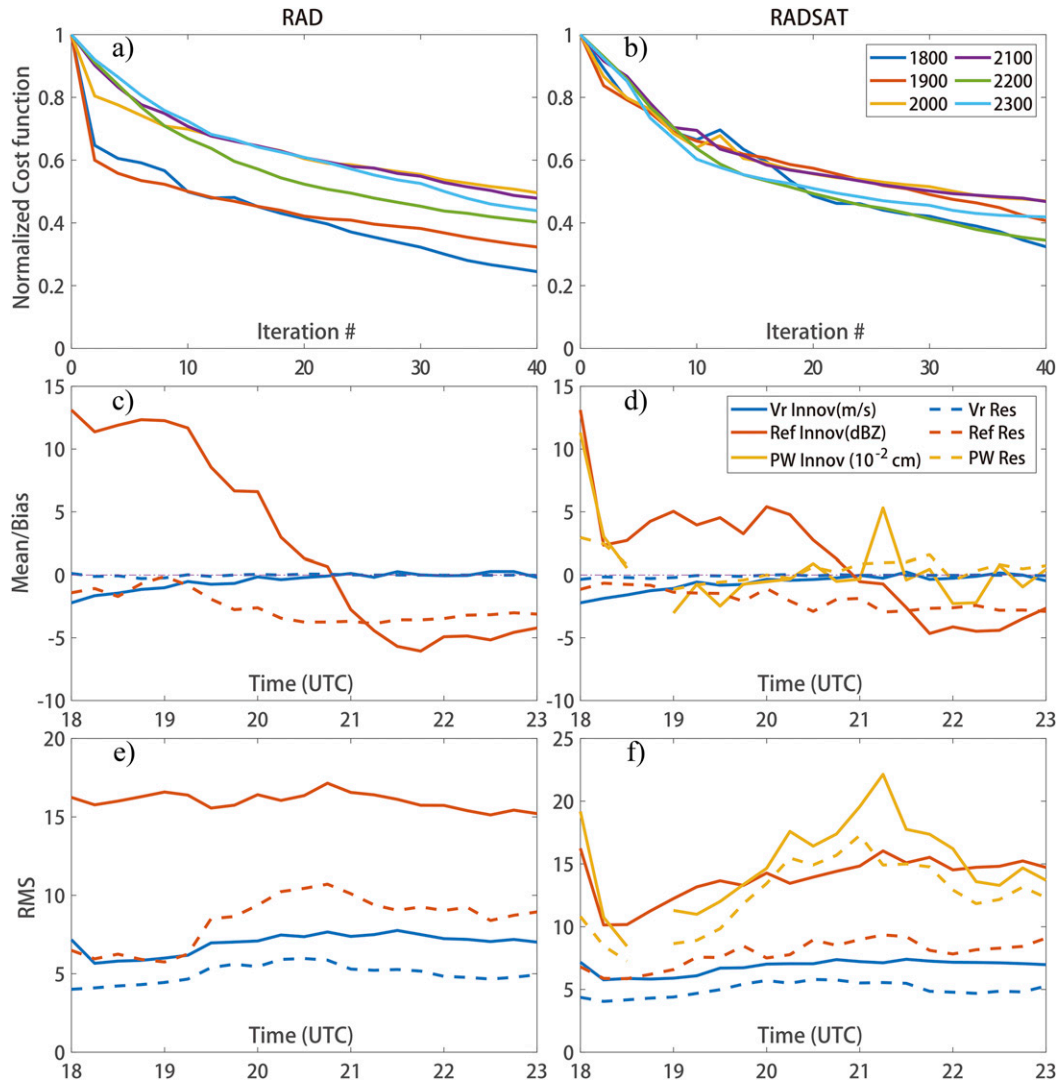


FIG. 17. (a),(b) Normalized cost function as a function of iteration number for the RAD and RADSAT experiments. The cost function curves are shown in colors for different analysis times following the legends in (b). (c),(d) Mean for the innovation (solid lines) and analysis residual (dashed lines) for radial velocity (blue, in m s^{-1}), reflectivity (red, in dBZ), and precipitable water (yellow, in 10^{-2} cm) as a function of analysis time for the RAD and RADSAT experiments. Dash-dotted lines in (c) and (d) are the reference lines for measuring biases. (e),(f) As in (c) and (d), RMS for the innovation and analysis residual are shown in for RAD and for RADSAT, respectively.

forecasts from RADSAT are better than those from the CTRL and RAD.

In spite of those encouraging results, some unwanted artifacts are also observed with the assimilation of CWP and LPW observations such as the development of spurious storm cells in the domain during the forecast. Another problem is the negative impact of the high layer precipitable water observations. More research is warranted to better determine whether such drawbacks can be addressed through either a quality control process for LPW product or improved background error covariances. More systematic experiments will be performed to investigate if these GOES satellite products have potential for better convective-scale analyses and forecasts in future real-time operations.

Acknowledgments. This research was funded by the NOAA Warn-on-Forecast project NA16OAR4320115 and NSF Grant AGS-1341878. Additional funding was provided by NOAA/Office of Oceanic and Atmospheric Research under the NOAA–University of Oklahoma Cooperative Agreement NA08OAR4320904. The SATCORPS cloud water path retrievals used in the Warn-on-Forecast system was kindly provided by NASA Langley Research Center.

REFERENCES

- Aksoy, A., D. C. Dowell, and C. Snyder, 2009: A multicase comparative assessment of the ensemble Kalman filter for assimilation of radar observations. Part I: Storm-scale analyses. *Mon. Wea. Rev.*, **137**, 1805–1824, <https://doi.org/10.1175/2008MWR2691.1>.

- Baldwin, M. E., and K. E. Mitchell, 1997: The NCEP hourly multi-sensor U.S. precipitation analysis for operations and GCIP research. Preprints, *13th Conf. on Hydrology*, Long Beach, CA, Amer. Meteor. Soc., 54–55.
- Benjamin, S. G., and Coauthors, 2004: An hourly assimilation–forecast cycle: The RUC. *Mon. Wea. Rev.*, **132**, 495–518, [https://doi.org/10.1175/1520-0493\(2004\)132<0495:AHACTR>2.0.CO;2](https://doi.org/10.1175/1520-0493(2004)132<0495:AHACTR>2.0.CO;2).
- Brewster, K., M. Hu, M. Xue, and J. Gao, 2005: Efficient assimilation of radar data at high resolution for short-range numerical weather prediction. *Int. Symp. on Nowcasting Very Short Range Forecasting*, Toulouse, France, WMO/World Weather Research Program, 3.06.
- Buehner, M., 2005: Ensemble-derived stationary and flow-dependent background-error covariances: Evaluation in a quasi-operational NWP setting. *Quart. J. Roy. Meteor. Soc.*, **131**, 1013–1043, <https://doi.org/10.1256/qj.04.15>.
- Chou, M. D., and M. J. Suarez, 1999: A solar radiation parameterization for atmospheric studies. NASA/TM-1999-104606, 40 pp.
- , —, X. Z. Liang, and M. M. H. Yan, 2001: A thermal infrared radiation parameterization for atmospheric studies. NASA/TM-2001-104606, 68 pp.
- Clark, A. J., M. Xue, and M. L. Weisman, 2010: Neighborhood-based verification of precipitation forecasts from convection-allowing NCAR WRF Model simulations and the operational NAM. *Wea. Forecasting*, **25**, 1495–1509, <https://doi.org/10.1175/2010WAF2222404.1>.
- Crum, T. D., R. L. Alberty, and D. W. Burgess, 1993: Recording, archiving, and using WSR-88D data. *Bull. Amer. Meteor. Soc.*, **74**, 645–653, [https://doi.org/10.1175/1520-0477\(1993\)074<0645:RAAUWD>2.0.CO;2](https://doi.org/10.1175/1520-0477(1993)074<0645:RAAUWD>2.0.CO;2).
- Dowell, D. C., and L. J. Wicker, 2009: Additive noise for storm-scale ensemble data assimilation. *J. Atmos. Oceanic Technol.*, **26**, 911–927, <https://doi.org/10.1175/2008JTECHA1156.1>.
- , F. Zhang, L. J. Wicker, C. Snyder, and N. A. Crook, 2004: Wind and temperature retrievals in the 17 May 1981 Arcadia, Oklahoma, supercell: Ensemble Kalman filter experiments. *Mon. Wea. Rev.*, **132**, 1982–2005, [https://doi.org/10.1175/1520-0493\(2004\)132<1982:WATRIT>2.0.CO;2](https://doi.org/10.1175/1520-0493(2004)132<1982:WATRIT>2.0.CO;2).
- , L. J. Wicker, and C. Snyder, 2011: Ensemble Kalman filter assimilation of radar observations of the 8 May 2003 Oklahoma city supercell: Influences of reflectivity observations on storm-scale analyses. *Mon. Wea. Rev.*, **139**, 272–294, <https://doi.org/10.1175/2010MWR3438.1>.
- Du, J., 2011: GCIP/EOP surface: Precipitation NCEP/EMC 4KM Gridded Data (GRIB) Stage IV Data, version 1.0. UCAR/NCAR–Earth Observing Laboratory, <https://doi.org/10.5065/D6PG1QDD>.
- Dudhia, J., 1989: Numerical study of convection observed during the winter monsoon experiment using a mesoscale two-dimensional model. *J. Atmos. Sci.*, **46**, 3077–3107, [https://doi.org/10.1175/1520-0469\(1989\)046<3077:NSOCOD>2.0.CO;2](https://doi.org/10.1175/1520-0469(1989)046<3077:NSOCOD>2.0.CO;2).
- Fierro, A. O., J. Gao, C. L. Ziegler, K. M. Calhoun, E. R. Mansell, and D. R. MacGorman, 2016: Assimilation of flash extent data in the variational framework at convection-allowing scales: Proof-of-concept and evaluation for the short-term forecast of the 24 May 2011 tornado outbreak. *Mon. Wea. Rev.*, **144**, 4373–4393, <https://doi.org/10.1175/MWR-D-16-0053.1>.
- , Y. Wang, J. Gao, and E. R. Mansell, 2019: Variational assimilation of radar data and GLM lightning-derived water vapor for the short-term forecasts of high-impact convective events. *Mon. Wea. Rev.*, **147**, 4045–4069, <https://doi.org/10.1175/MWR-D-18-0421.1>.
- Fujita, T., D. J. Stensrud, and D. C. Dowell, 2007: Surface data assimilation using an ensemble Kalman filter approach with initial condition and model physics uncertainties. *Mon. Wea. Rev.*, **135**, 1846–1868, <https://doi.org/10.1175/MWR3391.1>.
- Gao, J., and D. J. Stensrud, 2012: Assimilation of reflectivity data in a convective-scale, cycled 3DVAR framework with hydrometeor classification. *J. Atmos. Sci.*, **69**, 1054–1065, <https://doi.org/10.1175/JAS-D-11-0162.1>.
- , and —, 2014: Some observing system simulation experiments with a hybrid 3DVAR system for storm-scale radar data assimilation. *Mon. Wea. Rev.*, **142**, 3326–3346, <https://doi.org/10.1175/MWR-D-14-00025.1>.
- , M. Xue, A. Shapiro, and K. K. Droegemeier, 1999: A variational method for the analysis of three-dimensional wind fields from two Doppler radars. *Mon. Wea. Rev.*, **127**, 2128–2142, [https://doi.org/10.1175/1520-0493\(1999\)127<2128:AVMFTA>2.0.CO;2](https://doi.org/10.1175/1520-0493(1999)127<2128:AVMFTA>2.0.CO;2).
- , —, K. Brewster, F. Carr, and K. K. Droegemeier, 2002: New development of a 3DVAR system for a nonhydrostatic NWP model. Preprint, *15th Conf. on Numerical Weather Prediction/19th Conf. on Weather Analysis and Forecasting*, San Antonio, TX, Amer. Meteor. Soc., 339–341.
- , —, —, and K. K. Droegemeier, 2004: A three-dimensional variational data analysis method with recursive filter for Doppler radars. *J. Atmos. Oceanic Technol.*, **21**, 457–469, [https://doi.org/10.1175/1520-0426\(2004\)021<0457:ATVDAM>2.0.CO;2](https://doi.org/10.1175/1520-0426(2004)021<0457:ATVDAM>2.0.CO;2).
- , and Coauthors, 2013: A real-time weather-adaptive 3DVAR analysis system for severe weather detections and warnings. *Wea. Forecasting*, **28**, 727–745, <https://doi.org/10.1175/WAF-D-12-00093.1>.
- , C. Fu, D. J. Stensrud, and J. S. Kain, 2016: OSSEs for an ensemble 3DVAR data assimilation system with radar observations of convective storms. *J. Atmos. Sci.*, **73**, 2403–2426, <https://doi.org/10.1175/JAS-D-15-0311.1>.
- Hong, S., Y. Noh, and J. Dudhia, 2006: A new vertical diffusion package with an explicit treatment of entrainment processes. *Mon. Wea. Rev.*, **134**, 2318–2341, <https://doi.org/10.1175/MWR3199.1>.
- Hu, J., A. Fierro, Y. Wang, J. Gao, and E. R. Mansell, 2020: Exploring the assimilation of GLM-derived water vapor mass in a cycled 3DVAR framework for the short-term forecasts of high-impact convective events. *Mon. Wea. Rev.*, **148**, 1005–1028, <https://doi.org/10.1175/MWR-D-19-0198.1>.
- Hu, M., M. Xue, J. Gao, and K. Brewster, 2006: 3DVAR and cloud analysis with WSR-88D level-II data for the prediction of the Fort Worth, Texas, tornadic thunderstorms. Part II: Impact of radial velocity analysis via 3DVAR. *Mon. Wea. Rev.*, **134**, 699–721, <https://doi.org/10.1175/MWR3093.1>.
- Iacono, M. J., J. S. Delamere, E. J. Mlawer, M. W. Shephard, S. A. Clough, and W. D. Collins, 2008: Radiative forcing by long-lived greenhouse gases: Calculations with the AER radiative transfer models. *J. Geophys. Res.*, **113**, D13103, <https://doi.org/10.1029/2008JD009944>.
- Janjić, Z. I., 1994: The step-mountain eta coordinate model: Further developments of the convection, viscous sublayer, and turbulence closure schemes. *Mon. Wea. Rev.*, **122**, 927–945, [https://doi.org/10.1175/1520-0493\(1994\)122<0927:TSMCEM>2.0.CO;2](https://doi.org/10.1175/1520-0493(1994)122<0927:TSMCEM>2.0.CO;2).
- Johnson, A., X. Wang, J. R. Carley, L. J. Wicker, and C. Karstens, 2015: A comparison of multiscale GSI-based EnKF and 3DVAR data assimilation using radar and conventional observations for midlatitude convective-scale precipitation fore-

- casts. *Mon. Wea. Rev.*, **143**, 3087–3108, <https://doi.org/10.1175/MWR-D-14-00345.1>.
- Jones, T. A., and D. J. Stensrud, 2015: Assimilating cloud water path as a function of model cloud microphysics in an idealized simulation. *Mon. Wea. Rev.*, **143**, 2052–2081, <https://doi.org/10.1175/MWR-D-14-00266.1>.
- , —, P. Minnis, and R. Palikonda, 2013: Evaluation of a forward operator to assimilate cloud water path into WRF-DART. *Mon. Wea. Rev.*, **141**, 2272–2289, <https://doi.org/10.1175/MWR-D-12-00238.1>.
- , K. Knopfmeier, D. Wheatley, G. Creager, P. Minnis, and R. Palikonda, 2016: Storm-scale data assimilation and ensemble forecasting with the NSSL experimental Warn-on-Forecast system. Part II: Combined radar and satellite data experiments. *Wea. Forecasting*, **31**, 297–327, <https://doi.org/10.1175/WAF-D-15-0107.1>.
- , X. Wang, P. Skinner, A. Johnson, and Y. Wang, 2018: Assimilation of GOES-13 imager clear-sky water vapor ($6.5\ \mu\text{m}$) radiances into a Warn-on-Forecast system. *Mon. Wea. Rev.*, **146**, 1077–1107, <https://doi.org/10.1175/MWR-D-17-0280.1>.
- , and Coauthors, 2020: Assimilation of GOES-16 radiances and retrievals into the Warn-on-Forecast system. *Mon. Wea. Rev.*, **148**, 1829–1859, <https://doi.org/10.1175/MWR-D-19-0379.1>.
- Lin, Y., and K. E. Mitchell, 2005: The NCEP Stage II/IV hourly precipitation analyses: Development and applications. *19th Conf. on Hydrology*, San Diego, CA, Amer. Meteor. Soc., 1.2, https://ams.confex.com/ams/Annual2005/techprogram/paper_83847.htm.
- Lorenc, A. C., 2003: Modelling of error covariances by 4D-Var data assimilation. *Quart. J. Roy. Meteor. Soc.*, **129**, 3167–3182, <https://doi.org/10.1256/qj.02.131>.
- Lu, J., T. Feng, J. Li, Z. Cai, X. Xu, L. Li, and J. Li, 2019: Impact of assimilating Himawari-8 derived layered precipitable water with varying cumulus and microphysics parameterization schemes on the simulation of Typhoon Hato. *J. Geophys. Res. Atmos.*, **124**, 3050–3071, <https://doi.org/10.1029/2018JD029364>.
- McPherson, R. A., T. Walters, G. Wilke, L. Osborne, R. Hart, T. Incrocci, and T. Schmitt, 2007: Statewide monitoring of the mesoscale environment: A technical update on the Oklahoma Mesonet. *J. Atmos. Oceanic Technol.*, **24**, 301–321, <https://doi.org/10.1175/JTECH1976.1>.
- Menzel, W. P., and J. F. Purdom, 1994: Introducing GOES-I: The first of a new generation of geostationary operational environmental satellites. *Bull. Amer. Meteor. Soc.*, **75**, 757–781, [https://doi.org/10.1175/1520-0477\(1994\)075<0757:IGITFO>2.0.CO;2](https://doi.org/10.1175/1520-0477(1994)075<0757:IGITFO>2.0.CO;2).
- Minnis, P., and Coauthors, 2011: CERES edition-2 cloud property retrievals using TRMM VIRS and Terra and Aqua MODIS data—Part I: Algorithms. *IEEE Trans. Geosci. Remote Sens.*, **49**, 4374–4400, <https://doi.org/10.1109/TGRS.2011.2144601>.
- Mlawer, E., S. Taubman, P. Brown, M. Iacono, and S. Clough, 1997: Radiative transfer for inhomogeneous atmospheres: RRTM, a validated correlated-k model for the longwave. *J. Geophys. Res.*, **102**, 16 663–16 682, <https://doi.org/10.1029/97JD00237>.
- Nakanishi, M., 2001: Improvement of the Mellor–Yamada turbulence closure model based on large-eddy simulation data. *Bound.-Layer Meteor.*, **99**, 349–378, <https://doi.org/10.1023/A:1018915827400>.
- , and H. Niino, 2004: An improved Mellor–Yamada level-3 model with condensation physics: Its design and verification. *Bound.-Layer Meteor.*, **112**, 1–31, <https://doi.org/10.1023/B:BOUN.0000020164.04146.98>.
- Pan, S., J. Gao, D. J. Stensrud, X. Wang, and T. A. Jones, 2018: Assimilation of radar radial velocity and reflectivity, satellite cloud water path, and total precipitable water for convective-scale NWP in OSSEs. *J. Atmos. Oceanic Technol.*, **35**, 67–89, <https://doi.org/10.1175/JTECH-D-17-0081.1>.
- Parker, M. D., 2014: Composite VORTEX2 supercell environments from near-storm soundings. *Mon. Wea. Rev.*, **142**, 508–529, <https://doi.org/10.1175/MWR-D-13-00167.1>.
- Purser, R. J., W.-S. Wu, D. Parrish, and N. M. Roberts, 2003: Numerical aspects of the application of recursive filters to variational statistical analysis. Part I: Spatially homogeneous and isotropic Gaussian covariances. *Mon. Wea. Rev.*, **131**, 1524–1535, [https://doi.org/10.1175/1520-0493\(2003\)131<1524:NAOTAO>2.0.CO;2](https://doi.org/10.1175/1520-0493(2003)131<1524:NAOTAO>2.0.CO;2).
- Roberts, N. M., and H. W. Lean, 2008: Scale-selective verification of rainfall accumulations from high-resolution forecasts of convective events. *Mon. Wea. Rev.*, **136**, 78–97, <https://doi.org/10.1175/2007MWR2123.1>.
- Schmit, T. J., E. M. Prins, A. J. Schreiner, and J. J. Gurka, 2001: Introducing the GOES-M imager. *Natl. Wea. Assoc. Digest*, **25**, 28–37.
- , M. M. Gunshor, W. P. Menzel, J. J. Gurka, J. Li, and A. S. Bachmeier, 2005: Introducing the next-generation Advanced Baseline Imager (ABI) on GOES-R. *Bull. Amer. Meteor. Soc.*, **86**, 1079–1096, <https://doi.org/10.1175/BAMS-86-8-1079>.
- , P. Griffith, M. M. Gunshor, J. M. Daniels, S. J. Goodman, and W. J. Lebar, 2017: A closer look at the ABI on the GOES-R series. *Bull. Amer. Meteor. Soc.*, **98**, 681–698, <https://doi.org/10.1175/BAMS-D-15-00230.1>.
- , and Coauthors, 2019: Legacy atmospheric profiles and derived products from GOES-16: Validation and applications. *Earth Space Sci.*, **6**, 1730–1748, <https://doi.org/10.1029/2019EA000729>.
- Skamarock, W. C., and Coauthors, 2008: A description of the Advanced Research WRF version 3. NCAR Tech. Note NCAR/TN-475+STR, 113 pp., <https://doi.org/10.5065/D68S4MVH>.
- Skinner, P. S., and Coauthors, 2018: Object-based verification of a prototype Warn-on-Forecast system. *Wea. Forecasting*, **33**, 1225–1250, <https://doi.org/10.1175/WAF-D-18-0020.1>.
- Smith, T. L., S. G. Benjamin, J. M. Brown, S. Weygandt, T. Smirnova, and B. Schwartz, 2008: Convection forecasts from the hourly updated, 3-km High Resolution Rapid Refresh Model. *24th Conf. on Severe Local Storms*, Savannah, GA, Amer. Meteor. Soc., 11.1, https://ams.confex.com/ams/24SLS/techprogram/paper_142055.htm.
- Smith, T. M., and Coauthors, 2016: Multi-Radar Multi-Sensor (MRMS) severe weather and aviation products: Initial operating capabilities. *Bull. Amer. Meteor. Soc.*, **97**, 1617–1630, <https://doi.org/10.1175/BAMS-D-14-00173.1>.
- Stensrud, D. J., and J. Gao, 2010: Importance of horizontally inhomogeneous environmental initial conditions to ensemble storm-scale radar data assimilation and very short-range forecasts. *Mon. Wea. Rev.*, **138**, 1250–1272, <https://doi.org/10.1175/2009MWR3027.1>.
- , J. Bao, and T. T. Warner, 2000: Using initial condition and model physics perturbations in short-range ensemble simulations of mesoscale convective systems. *Mon. Wea. Rev.*, **128**, 2077–2107, [https://doi.org/10.1175/1520-0493\(2000\)128<2077:UICAMP>2.0.CO;2](https://doi.org/10.1175/1520-0493(2000)128<2077:UICAMP>2.0.CO;2).
- Sun, J., 2005: Initialization and numerical forecasting of a supercell storm observed during STEPS. *Mon. Wea. Rev.*, **133**, 793–813, <https://doi.org/10.1175/MWR2887.1>.
- Thompson, G., R. M. Rasmussen, and K. Manning, 2004: Explicit forecasts of winter precipitation using an improved bulk microphysics scheme. Part I: Description and sensitivity analysis. *Mon. Wea. Rev.*, **132**, 519–542, [https://doi.org/10.1175/1520-0493\(2004\)132<0519:EFOWPU>2.0.CO;2](https://doi.org/10.1175/1520-0493(2004)132<0519:EFOWPU>2.0.CO;2).

- , P. R. Field, R. M. Rasmussen, and W. D. Hall, 2008: Explicit forecasts of winter precipitation using an improved bulk microphysics scheme. Part II: Implementation of a new snow parameterization. *Mon. Wea. Rev.*, **136**, 5095–5115, <https://doi.org/10.1175/2008MWR2387.1>.
- Wang, P., J. Li, B. Lu, T. J. Schmit, J. Lu, Y.-K. Lee, J. Li, and Z. Liu, 2018: Impact of moisture information from Advanced Himawari Imager measurements on heavy precipitation forecasts in a regional NWP model. *J. Geophys. Res. Atmos.*, **123**, 6022–6038, <https://doi.org/10.1029/2017JD028012>.
- Wang, X., C. Snyder, and T. M. Hamill, 2007: On the theoretical equivalence of differently proposed ensemble/3D-Var hybrid analysis schemes. *Mon. Wea. Rev.*, **135**, 222–227, <https://doi.org/10.1175/MWR3282.1>.
- , D. M. Barker, C. Snyder, and T. M. Hamill, 2008: A hybrid ETKF–3DVAR data assimilation scheme for the WRF model. Part I: Observing system simulation experiment. *Mon. Wea. Rev.*, **136**, 5116–5131, <https://doi.org/10.1175/2008MWR2444.1>.
- , D. Parrish, D. Kleist, and J. S. Whitaker, 2013: GSI 3DVar-based ensemble–variational hybrid data assimilation for NCEP Global Forecast System: Single-resolution experiments. *Mon. Wea. Rev.*, **141**, 4098–4117, <https://doi.org/10.1175/MWR-D-12-00141.1>.
- Wang, Y., and X. Wang, 2017: Direct assimilation of radar reflectivity without tangent linear and adjoint of the nonlinear observation operator in the GSI-based EnVar system: Methodology and experiment with the 8 May 2003 Oklahoma City tornadic supercell. *Mon. Wea. Rev.*, **145**, 1447–1471, <https://doi.org/10.1175/MWR-D-16-0231.1>.
- , J. Gao, P. S. Skinner, K. Knopfmeier, T. Jones, G. Creager, P. L. Heiselman, and L. J. Wicker, 2019: Test of a weather-adaptive dual-resolution hybrid Warn-on-Forecast analysis and forecast system for several severe weather events. *Wea. Forecasting*, **34**, 1807–1827, <https://doi.org/10.1175/WAF-D-19-0071.1>.
- Weisman, M. L., and J. B. Klemp, 1982: The dependence of numerically simulated convective storms on vertical wind shear and buoyancy. *Mon. Wea. Rev.*, **110**, 504–520, [https://doi.org/10.1175/1520-0493\(1982\)110<0504:TDONSC>2.0.CO;2](https://doi.org/10.1175/1520-0493(1982)110<0504:TDONSC>2.0.CO;2).
- Wheatley, D. M., N. Yussouf, and D. J. Stensrud, 2014: Ensemble Kalman filter analyses and forecasts of a severe mesoscale convective system using different choices of microphysics schemes. *Mon. Wea. Rev.*, **142**, 3243–3263, <https://doi.org/10.1175/MWR-D-13-00260.1>.
- , K. H. Knopfmeier, T. A. Jones, and G. J. Creager, 2015: Storm-scale data assimilation and ensemble forecasting with the NSSL experimental Warn-on-Forecast system. Part I: Radar data experiments. *Wea. Forecasting*, **30**, 1795–1817, <https://doi.org/10.1175/WAF-D-15-0043.1>.
- Whitaker, J. S., and T. M. Hamill, 2002: Ensemble data assimilation without perturbed observations. *Mon. Wea. Rev.*, **130**, 1913–1924, [https://doi.org/10.1175/1520-0493\(2002\)130<1913:EDAWPO>2.0.CO;2](https://doi.org/10.1175/1520-0493(2002)130<1913:EDAWPO>2.0.CO;2).
- Yussouf, N., and D. J. Stensrud, 2010: Impact of phased-array radar observations over a short assimilation period: Observing system simulation experiments using an ensemble Kalman filter. *Mon. Wea. Rev.*, **138**, 517–538, <https://doi.org/10.1175/2009MWR2925.1>.
- , and K. H. Knopfmeier, 2019: Application of the Warn-on-Forecast system for flash-flood-producing heavy convective rainfall events. *Quart. J. Roy. Meteor. Soc.*, **145**, 2385–2403, <https://doi.org/10.1002/qj.3568>.
- , E. R. Mansell, L. J. Wicker, D. M. Wheatley, and D. J. Stensrud, 2013: The ensemble Kalman filter analyses and forecasts of the 8 May 2003 Oklahoma City tornadic supercell storm using single- and double-moment microphysics schemes. *Mon. Wea. Rev.*, **141**, 3388–3412, <https://doi.org/10.1175/MWR-D-12-00237.1>.
- Zhang, Y., D. J. Stensrud, and F. Zhang, 2019: Simultaneous assimilation of radar and all-sky satellite infrared radiance observations for convection-allowing ensemble analysis and prediction of severe thunderstorms. *Mon. Wea. Rev.*, **147**, 4389–4409, <https://doi.org/10.1175/MWR-D-19-0163.1>.
- Zhou, X., Y. Zhu, D. Hou, Y. Luo, J. Peng, and D. Wobus, 2017: Performance of the new NCEP global ensemble forecast system in a parallel experiment. *Wea. Forecasting*, **32**, 1989–2004, <https://doi.org/10.1175/WAF-D-17-0023.1>.